

Self-Aware Object Detection via Degradation Manifolds

Stefan Becker  

Simon Weiss  

Wolfgang Hübner  

Michael Arens  

arXiv:2602.18394v1 [cs.CV] 20 Feb 2026

Abstract

Object detectors achieve strong performance under nominal imaging conditions but can fail silently when exposed to blur, noise, compression, adverse weather, or resolution changes. In safety-critical settings, it is therefore insufficient to produce predictions without assessing whether the input remains within the detector’s nominal operating regime. We refer to this capability as *self-aware object detection*.

We introduce a degradation-aware self-awareness framework based on *degradation manifolds*, which explicitly structure a detector’s feature space according to image degradation rather than semantic content. Our method augments a standard detection backbone with a lightweight embedding head trained via multi-layer contrastive learning. Images sharing the same degradation composition are pulled together, while differing degradation configurations are pushed apart, yielding a geometrically organized representation that captures degradation type and severity without requiring degradation labels or explicit density modeling.

To anchor the learned geometry, we estimate a pristine prototype from clean training embeddings, defining a nominal operating point in representation space. Self-awareness emerges as geometric deviation from this reference, providing an intrinsic, image-level signal of degradation-induced shift that is independent of detection confidence.

Extensive experiments on synthetic corruption benchmarks, cross-dataset zero-shot transfer, and natural weather-induced distribution shifts demonstrate strong pristine–degraded separability, consistent behavior across multiple detector architectures, and robust generalization under semantic shift. These results suggest that degradation-aware representation geometry provides a practical and detector-agnostic foundation for self-aware object detection.

Contents

1	Introduction	4
2	Related Work	6
3	Method	8
3.1	Multi-Layer Degradation Representation	8
3.2	Contrastive Degradation Manifold Learning	9
3.3	Pristine Prototype and Degradation Score	10
3.4	Auxiliary Monitoring Branch	10
4	Evaluation	11
4.1	Dataset and Degradation Benchmark	11
4.2	Models and Compared Monitors	11
4.3	Metrics	12
4.4	Results	12
4.4.1	Detector Performance	12
4.4.2	Degradation Manifold Analysis.	12
4.4.3	Self-Awareness under Degradation	14
5	Discussion and Limitations	18
6	Conclusion	19
	Supplementary Material	25
	Detectors	25
	Datasets	28
	Evaluation	29
	Joint Detection–Degradation Training Study	36
	Training	38

1. Introduction

Modern object detectors achieve strong performance when imaging conditions match those seen during training. However, in real-world deployments, image quality can vary substantially due to noise, blur, compression, adverse weather, or resolution changes. Under such degradations, detectors may fail silently: predictions can remain confident even when visual evidence has deteriorated [43, 36]. In safety-critical and unconstrained environments, it is therefore insufficient to produce predictions without assessing whether the input remains within the detector’s nominal operating regime. We refer to this capability as *self-aware object detection*.

A common strategy to estimate reliability is to rely on confidence scores or predictive uncertainty. While effective under mild perturbations, these signals are inherently tied to prediction outcomes and may break down under strong image degradation. Severely degraded inputs may yield sparse or no detections, often accompanied by high confidence in the absence of objects. Crucially, the absence of detections does not imply reliable perception. This exposes a fundamental limitation of output-based indicators: they do not directly assess the quality of the underlying representation.

To reason about reliability independently of prediction content, we consider a degradation-aware formulation:

$$P(\mathbf{y} \mid \mathbf{x}, \mathcal{D})_{\text{deg}} = P(\mathbf{y} \mid \mathbf{x}, \mathcal{D}) \cdot P_{\text{deg}}(\mathbf{x}), \quad (1)$$

where \mathbf{y} denotes the detector output, \mathbf{x} the input image, and \mathcal{D} the training data. The term $P_{\text{deg}}(\mathbf{x})$ captures whether the input lies within a regime of acceptable visual quality. Importantly, we assume that no failure-labeled or unsafe samples are available during training, reflecting realistic deployment constraints.

Most existing approaches to estimating $P_{\text{deg}}(\mathbf{x})$ are formulated as out-of-distribution (OoD) detection. However, OoD methods were primarily developed for classification and transfer imperfectly to object detection. Detection produces dense, structured outputs rather than a single global prediction, and OoD signals derived from logits or class scores tend to capture semantic novelty rather than input degradation [9].

Moreover, likelihood-based OoD models are often sensitive to dataset identity and scene content rather than image fidelity. They may assign low likelihood to clean but novel scenes, while assigning relatively high likelihood to severely degraded images whose low-level statistics resemble the training distribution [42, 57]. Recent analyses further show that modern vision models encode strong dataset-specific signatures [31], increasing the risk that likelihood-based signals conflate source differences with reliability.

These observations reveal a mismatch between semantic OoD detection and degradation-driven reliability assessment. In practice, many detector failures arise not from novel objects, but from progressive loss of visual fidelity. Such shifts are continuous and largely independent of semantic content. We therefore use the term *image degradation* as an umbrella concept encompassing corruptions, distortions, and artifacts that deviate from ideal image formation.

Recent advances in no-reference image quality assessment (IQA) demonstrate that degradation-aware representations can be learned without explicit supervision. Contrastive methods such as ARNIQA [1] show that multiple degraded views of the same image can be embedded into a structured representation space encoding degradation type and severity. These findings suggest that degradation induces coherent geometric structure in feature space.

Inspired by this observation, we propose to equip object detectors with degradation-aware representations. We augment a detector backbone with a degradation-aware embedding head trained via multi-layer contrastive learning. Images sharing the same degradation composition are pulled together, while embeddings corresponding to different degradation configurations are pushed apart. This yields a *degradation manifold* embedded within the detector’s feature space, explicitly organizing representations according to image fidelity rather than semantic content.

To anchor the manifold, we compute a pristine prototype from clean embeddings, defining a nominal operating point in representation space. Self-awareness is obtained as geometric deviation from this ref-

erence, providing an intrinsic image-level signal of degradation-induced input shift that is independent of detection confidence.

By explicitly modeling degradation structure within task-aligned representations, our approach addresses a complementary and practically relevant failure mode of object detectors. In the remainder of this paper, we present the degradation manifold framework and demonstrate through extensive experiments that degradation-aware representation geometry provides consistent separability under diverse corruptions and natural weather shifts. Viewed in this way, degradation-aware self-awareness is not an IQA problem, but a representation learning problem for reliable perception.

2. Related Work

OoD Detection and Reliability in Object Detection. Most approaches to estimating input validity are framed as out-of-distribution (OoD) detection. However, the majority of OoD methods were developed for classification, where each input yields a single global prediction. These methods typically operate on penultimate-layer features, logits, or softmax scores, including *maximum softmax probability* (MSP) [18], ODIN [27], *GradNorm* [20], *ReAct* [46], and energy-based approaches [30].

In object detection, predictions are defined at the detection level across many spatial locations or queries. Consequently, OoD signals derived from logits or class scores primarily capture semantic novelty (e.g., open-set detection [9]) rather than providing a reliable image-level assessment of imaging conditions. Constraint-based runtime monitors that verify geometric or logical consistency [22, 6] address complementary system-level properties and are orthogonal to our focus on degradation-driven shift.

Semantic OoD versus Degradation-Driven Shift. A fundamental limitation of many OoD formulations is their sensitivity to image content rather than image quality. Likelihood-based models, in particular, may assign low likelihood to clean images from new scenes while assigning comparatively high likelihood to severely degraded images whose low-level statistics resemble the training distribution [40, 25]. This behavior has been widely observed in generative OoD models [42].

Such effects reveal a mismatch between semantic OoD detection and degradation-driven reliability assessment. In practice, detector failures often arise from progressive loss of visual fidelity rather than semantic novelty. These shifts are continuous, structured, and largely independent of scene content. Throughout this work, we use the term *image degradation* to encompass corruptions, distortions, and artifacts that deviate from ideal image formation and progressively affect task-relevant information.

Generative Models for OoD Detection. Generative approaches estimate likelihood under a learned data distribution. *Variational autoencoders* [24] approximate likelihood via the ELBO, while *normalizing flows* (NFs) [26] provide exact and tractable densities. However, image-level likelihood is known to be an unreliable indicator of OoD [40]. Recent work mitigates this by modeling multi-layer feature activations rather than raw pixels [47, 32]. We adopt feature-level NFs as a baseline, but note that density modeling captures distributional similarity and does not explicitly disentangle degradation from semantic variation.

Uncertainty Estimation in Object Detection. Detection-level uncertainty aims to quantify predictive uncertainty through probabilistic modeling. Exact Bayesian inference is intractable [34], and practical approximations include MC dropout [12] and variance networks [23]. Variance networks parameterize predictive distributions and are trained with scoring rules such as negative log-likelihood, energy score [14], or direct moment matching [10]. While effective for modeling predictive uncertainty, these methods operate at the detection level. Image-level aggregation (e.g., top- k uncertainty [41]) provides a coarse proxy but remains tied to detection outcomes rather than directly assessing input fidelity.

Robust Object Detection under Image Degradation. Robustness of detectors to common corruptions has been extensively studied, revealing significant performance drops under noise, blur, weather effects, and compression [36, 55]. These works primarily aim to improve robustness via augmentation or architectural modifications. In contrast, we focus on enabling detectors to assess their operating regime at test time without requiring failure supervision.

Image Quality Assessment. Image quality assessment (IQA) models degradation from the perspective of human perceptual quality. Classical full-reference metrics such as SSIM [52] and FSIM [58], and no-reference methods such as BRISQUE [37] and NIQE [38], estimate perceptual fidelity. Recent learning-based approaches, including contrastive methods such as ARNIQA [1], demonstrate that degradations induce structured geometry in feature space.

While conceptually related, IQA optimizes perceptual scoring rather than deployment-time reliability monitoring. In contrast, we learn degradation-aware representations directly within a detector backbone and anchor them to nominal operating conditions. Our goal is not to estimate perceptual quality, but to structure representation geometry such that deviation from clean operating regimes becomes measurable.

3. Method

We aim to learn a *degradation-aware representation* within a detector architecture that organizes images according to image degradation rather than semantic content. To this end, we attach a lightweight embedding head to selected backbone layers and shape the feature space to encode structured degradation geometry. Depending on the training configuration, backbone layers may optionally be fine-tuned. However, in our main experiments we employ an auxiliary monitoring branch operating alongside a standard detector.

The resulting degradation manifold is designed to: (i) separate different degradation types and severities, (ii) map images with identical degradation characteristics consistently despite nuisance factors such as scale or resolution, and (iii) be geometrically oriented with respect to clean operating conditions to enable distance-based reliability estimation.

We adopt the degradation-aware formulation introduced earlier,

$$P(\mathbf{y} \mid \mathbf{x}, \mathcal{D})_{\text{deg}} = P(\mathbf{y} \mid \mathbf{x}, \mathcal{D}) \cdot P_{\text{deg}}(\mathbf{x}), \quad (2)$$

and approximate $P_{\text{deg}}(\mathbf{x})$ by a geometry-derived score $S_{\text{deg}}(\mathbf{x})$ computed as a distance in a learned embedding space. The score serves as a monotonic proxy for degradation severity without explicit density estimation or likelihood modeling.

At deployment, a monitoring decision is obtained via

$$\hat{r}(\mathbf{x}) = \mathbb{I}[S_{\text{deg}}(\mathbf{x}) \leq \tau], \quad (3)$$

where τ defines the acceptable degradation regime. An overview of the framework is shown in Fig. 1.

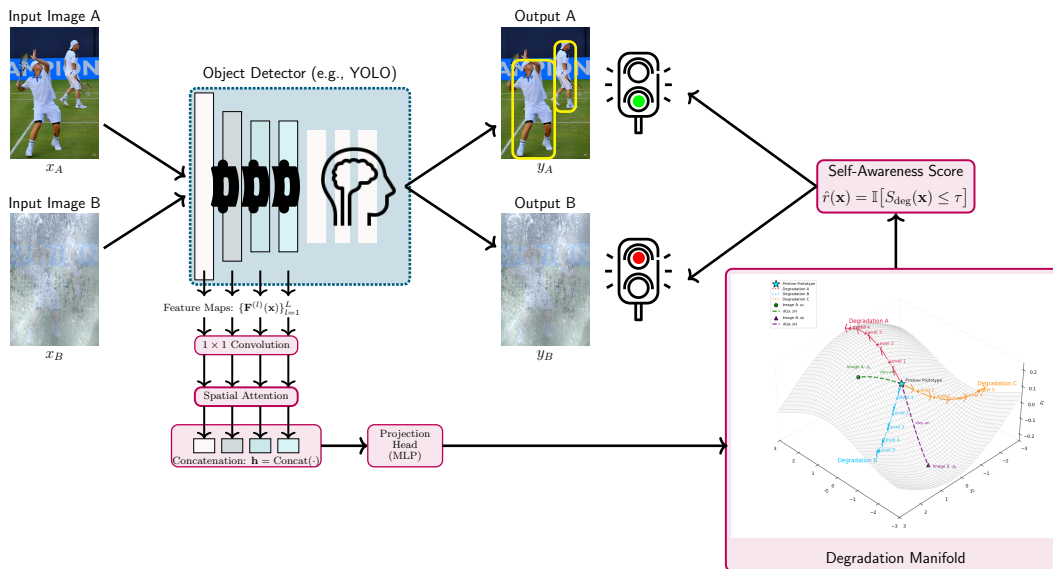


Figure 1: Proposed degradation-manifold framework for self-awareness. Multi-layer backbone features are fused via 1×1 projections and attention pooling and mapped into a normalized embedding space trained with contrastive degradation compositions. A pristine prototype, computed from clean training images, anchors the manifold to nominal operating conditions. At inference, cosine distance to this prototype yields the image-level degradation score $S_{\text{deg}}(\mathbf{x})$.

3.1 Multi-Layer Degradation Representation

Deep convolutional detectors exhibit hierarchical feature representations: shallow layers encode local textures and high-frequency statistics, while deeper layers capture increasingly abstract and semantic

information. Image degradations affect these layers differently. Low-level corruptions such as blur or noise perturb early features directly, whereas severe degradations propagate into higher-level representations and alter contextual encoding. Prior work shows that individual CNN layers possess distinct capabilities in separating degradation types and severities, and that multi-layer fusion improves distortion analysis [51, 3].

Accordingly, we extract feature maps from multiple backbone stages,

$$\{\mathbf{F}^{(l)}(\mathbf{x})\}_{l=1}^L.$$

Each feature map is reduced via a 1×1 convolution and pooled using a learnable attention-based operator, producing vectors $\mathbf{a}^{(l)} \in \mathbb{R}^d$. The per-layer vectors are concatenated to form a multi-scale descriptor

$$\mathbf{h} = \text{Concat}(\mathbf{a}^{(1)}, \dots, \mathbf{a}^{(L)}), \quad (4)$$

capturing complementary degradation cues across depths. In practice, we use early backbone stages together with later feature hierarchy outputs.

The fused representation is projected into a low-dimensional embedding space via a lightweight MLP,

$$\mathbf{z} = g(\mathbf{h}) \in \mathbb{R}^D, \quad (5)$$

followed by ℓ_2 normalization.

3.2 Contrastive Degradation Manifold Learning

To organize embeddings according to degradation composition and severity, we adopt a SimCLR-style contrastive objective [5], inspired by the degradation chaining strategy of ARNIQA [1].

For each clean image \mathbf{x} , we generate degraded views by sampling a composition

$$C_i = \{d_1, \dots, d_k\},$$

where each d_j denotes a degradation operator (e.g., blur, noise, compression) applied with randomly sampled parameters. Sequential compositions produce structured and progressively stronger perturbations without requiring degradation labels.

Given two pristine images degraded with the same sampled composition C_i , we obtain a positive pair $(z_{i,A}, z_{i,B})$. To encourage finer regime separation, we additionally construct hard negatives by applying an extra resolution perturbation: degraded images are center-cropped to half spatial resolution and resized back to the detector input size before encoding. Since this introduces resolution-induced fidelity loss while preserving semantic content, embeddings of full-resolution degraded views and their rescaled counterparts form hard negative pairs.

For a batch of size N_B , we optimize the NT-Xent objective

$$\mathcal{L}_{\text{deg}} = \frac{1}{4N_B} \sum_{i=1}^{N_B} \left(\ell(z_{i,A}, z_{i,B}) + \ell(z_{i,B}, z_{i,A}) + \ell(z_{i,\tilde{A}}, z_{i,\tilde{B}}) + \ell(z_{i,\tilde{B}}, z_{i,\tilde{A}}) \right), \quad (6)$$

where $\ell(\cdot, \cdot)$ denotes the standard NT-Xent loss with temperature τ_c , and negatives are drawn from all remaining embeddings in the batch, including cross-scale counterparts.

This objective encourages separation between degradation regimes while maintaining consistency for identical compositions. Because negatives include semantically diverse images, the learned geometry becomes largely content-independent and aligned with degradation characteristics. Unlike ARNIQA, which learns an encoder for perceptual quality regression, we integrate the degradation manifold into the detector architecture for reliability monitoring rather than quality score prediction.

3.3 Pristine Prototype and Degradation Score

Contrastive learning structures relative geometry but does not define a nominal reference. To orient the manifold with respect to clean operating conditions, we maintain a pristine prototype $\boldsymbol{\mu}_{\text{pristine}}$ computed from embeddings of pristine images.

To avoid instability during early contrastive training, the pristine prototype is not updated from the beginning of optimization. Instead, we initialize $\boldsymbol{\mu}_{\text{pristine}}$ after a warm-up phase (half of the total training epochs), once the embedding space has reached a sufficiently structured geometry. This prevents the prototype from being biased by poorly structured early embeddings.

The prototype is updated via an exponential moving average:

$$\boldsymbol{\mu}_{\text{pristine}} \leftarrow \alpha \boldsymbol{\mu}_{\text{pristine}} + (1 - \alpha) \mathbb{E}[\mathbf{z}_{\text{pristine}}], \quad (7)$$

with momentum $\alpha \in [0, 1)$ and without gradient propagation.

At inference time, we define the degradation score as the cosine distance to the pristine prototype:

$$S_{\text{deg}}(\mathbf{x}) = 1 - \frac{\mathbf{z}(\mathbf{x})^\top \boldsymbol{\mu}_{\text{pristine}}}{\|\mathbf{z}(\mathbf{x})\|_2 \|\boldsymbol{\mu}_{\text{pristine}}\|_2}. \quad (8)$$

Since embeddings are ℓ_2 -normalized, this simplifies to

$$S_{\text{deg}}(\mathbf{x}) = 1 - \mathbf{z}(\mathbf{x})^\top \boldsymbol{\mu}_{\text{pristine}}.$$

Larger values indicate increasing deviation from nominal imaging conditions. The score therefore provides an intrinsic, geometry-based estimate of degradation shift without explicit likelihood modeling.

3.4 Auxiliary Monitoring Branch

The degradation manifold can in principle be optimized jointly with the detection objective. However, contrastive degradation learning encourages sensitivity to fidelity changes, whereas detection training promotes invariance to nuisance variation. Joint optimization therefore introduces a trade-off between degradation separability and detection accuracy.

In our main experiments, we adopt an auxiliary two-path configuration, analogous to generative and IQA-based monitors, where the degradation head operates alongside a standard detector without replacing its robustness objective. This preserves detection performance while enabling degradation-aware monitoring. Joint training results and analysis of the trade-off are provided in Appendix 6.

4. Evaluation

We evaluate self-aware detection by analyzing whether degradation-induced covariate shift can be reliably detected at the image level and how this relates to task performance under shift. Our objective is not to predict per-instance detection correctness, but to identify deviations from nominal operating conditions. Following established practice in OoD and robustness evaluation, we measure *pristine vs. degraded separability* using AUROC. To contextualize monitoring performance, we additionally report the degradation-induced drop in detection accuracy (mAP).

4.1 Dataset and Degradation Benchmark

Our primary benchmark is COCO [28]. The training split is used to train detectors and baseline monitors and to compute pristine reference prototypes. The unaltered validation set serves as the in-distribution (ID) reference.

To simulate degradation-induced covariate shift in $p(\mathbf{x})$ [43], we apply synthetic degradations from the robustness suite of Michaelis et al. [36] (based on Hendrycks and Dietterich [17]). Each corruption is evaluated at five severity levels, producing progressively degraded splits with unchanged labels.

Evaluation degradations are *not identical* to those used during contrastive training of the degradation manifold. Training uses degradation compositions inspired by Agnolucci et al. [1], whereas evaluation follows robustness-style corruptions ([17, 36]). While some degradation *families* (e.g., blur or noise) overlap conceptually, the concrete operators, parameterizations, and severity schedules differ, and we perform no degradation-specific tuning, threshold selection, or calibration on the evaluation corruptions. Results therefore reflect generalization across corruption parameterizations and degradation regimes beyond the exact transformations observed during training.

For multi-corruption evaluation, we use a round-robin assignment scheme such that each image is consistently associated with a specific corruption across severity levels.

4.2 Models and Compared Monitors

Detector Backbones and Degradation Manifold. Our degradation manifold is implemented as a lightweight embedding head attached to the feature hierarchy of a standard object detector. To assess detector dependence, we instantiate the method on multiple COCO-pretrained backbones: YOLOv9 [49], YOLOv10-m [48], YOLOv11 [21], and the transformer-based RT-DETR [60]. Details on architectures and training settings are provided in Appendix 6.

Backbone features are fine-tuned jointly with the degradation embedding head via multi-layer contrastive learning. At inference time, self-awareness is computed as cosine distance between the image embedding and a pristine prototype estimated from unaltered COCO training images, yielding an intrinsic image-level degradation signal in the detector’s representation space.

Probabilistic Detectors. We compare against image-level uncertainty derived from probabilistic detectors using top- k aggregation as proposed by Oksuz et al. [41]. Probabilistic detectors are realized as variance networks that extend standard detectors to output parameters of a multivariate Gaussian predictive distribution [15]. They are trained using scoring rules such as negative log-likelihood (NLL), energy score (ES) [14], and direct moment matching (DMM) [10].

We derive image-level monitoring scores from detector outputs: confidence scores and entropy of predictive class distributions, as well as determinant, trace, and entropy of the Gaussian box distributions [39]. Since aggregation depends on available detections, we do not apply a confidence threshold to filter predictions.

Generative Modeling We include a likelihood-based baseline using normalizing flows (NFs) trained on detector features (e.g., RealNVP [7]), following feature-space OoD modeling [33]. The monitoring signal

is negative log-likelihood, where pristine ID samples should yield higher likelihood (lower $-\log p$) than degraded samples.

We use RealNVP with four masked affine coupling blocks in two variants: (i) a single NF trained on concatenated multi-layer features and (ii) a multi-scale NF (M-NF) with one NF per layer and aggregated scores. Following Lotfi et al. [33], we use a ResNet backbone [16] with globally average pooled features. The score is $-\log p_{\text{deg/ID}}(\mathbf{x})$.

Image Quality Assessment Baselines. Modern no-reference IQA models learn representations structured by perceptual degradation, making them conceptually related to degradation monitoring. We therefore include representative IQA methods as comparison baselines. We evaluate IQA models in two ways: (i) their predicted quality scores as image-level monitoring signals, and (ii) their learned embeddings as geometric monitors by measuring cosine distance to a pristine prototype.

The prototype is computed as the mean embedding over clean COCO training images, following prototype-based representation learning and distance-based OoD detection [45, 35]. All IQA models are evaluated zero-shot on degraded COCO images without fine-tuning or calibration for detection.

4.3 Metrics

Self-Awareness under Degradation. We quantify monitor quality using the *area under receiver operating characteristic* (AUROC) between pristine validation images and degraded variants. Degraded samples are treated as the positive class, and all scores are oriented such that larger values indicate stronger deviation from pristine conditions. Scores include the negative log-likelihood $-\log p_{\text{deg/ID}}(x)$ for NFs, detector-derived signals (e.g., confidence, entropy), IQA scores, and cosine distance in embedding space. Final AUROC values are computed after z-score normalization [47].

Detection Performance under Degradation. To contextualize monitor behavior, we report standard detection metrics *mean average precision* (mAP@.5:.95 and mAP@0.5) under increasing severity. This analysis highlights that degradations reduce task performance, while detectors may still output high-confidence predictions, motivating the need for a separate degradation monitor.

4.4 Results

4.4.1 DETECTOR PERFORMANCE

Figure 2 shows the mAP drop under increasing corruption severity for multiple detectors on the mixed-degradation COCO val2017 benchmark. All detectors exhibit similar monotonic performance degradation as severity increases.

Figures 3 summarize per-corruption performance trends for degradations from Michaelis et al. [36] and Agnolucci et al. [1]. Across the evaluated set, robustness-style corruptions from [36, 17] generally induce stronger performance drops than IQA-motivated distortions [1]. This reflects their respective design goals: robustness corruptions are constructed to disrupt semantic and structural cues aggressively, whereas IQA distortions model visually plausible quality variations that may preserve object-level structure. Overall, detection performance degrades monotonically with increasing severity for most corruptions, consistent with prior robustness analyses for detection [41, 36, 29].

4.4.2 DEGRADATION MANIFOLD ANALYSIS.

Figures 4 and 5 visualize the learned embedding space using t-SNE [19]. Across both corruption taxonomies, degraded samples form clearly separated clusters by degradation type despite the absence of degradation labels during training, indicating that the representation is primarily organized by degradation characteristics rather than semantic content.

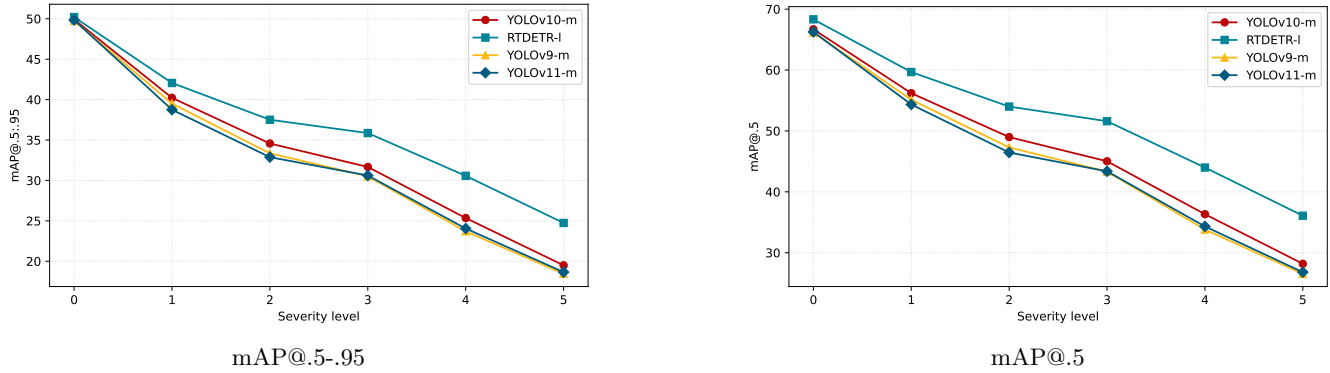


Figure 2: Detection performance (mAP@.5-.95 and mAP@.5) of different detection models under increasing corruption severity on the COCO val2017 dataset. Here the results of YOLOv9-m [49], YOLOv10-m [48], YOLOv11-m [21], and the transformer-based RT-DETR-l [60] are shown.

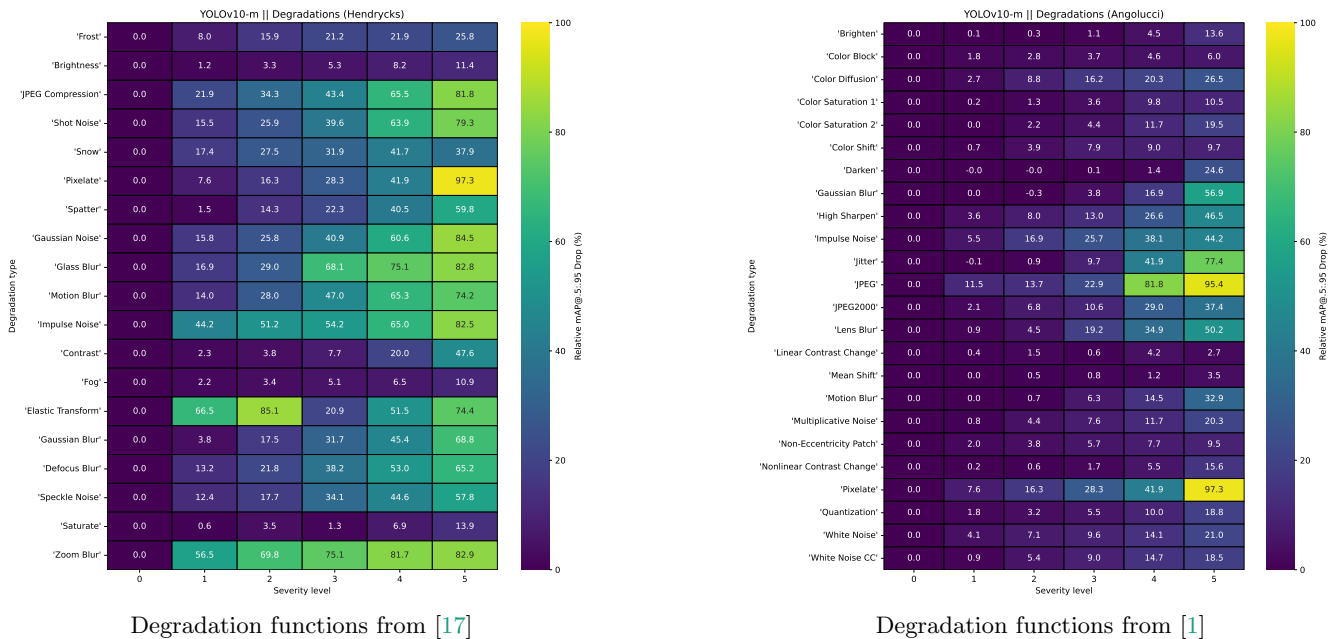
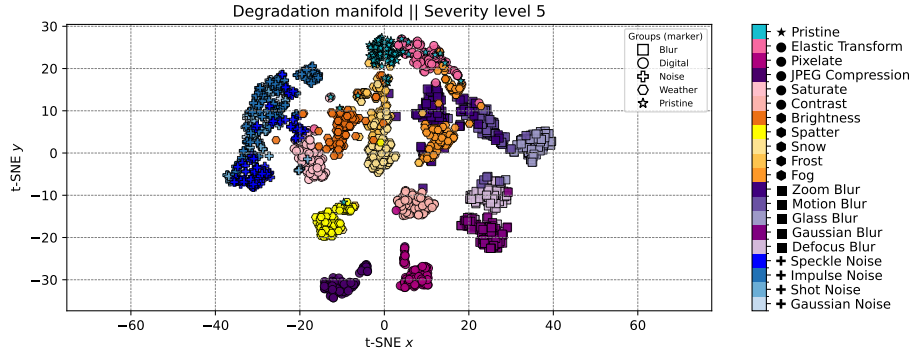


Figure 3: Relative detection performance drop of YOLOv10-m [48] on COCO val2017 under increasing native severity levels (mAP@0.5:0.95). Each cell shows the percentage drop relative to the clean val2017 baseline (pristine COCO images, no added degradations). Brighter cells indicate larger drops. Left: degradations from Michaelis et al. [36]. Right: degradations from Agnolucci et al. [1].

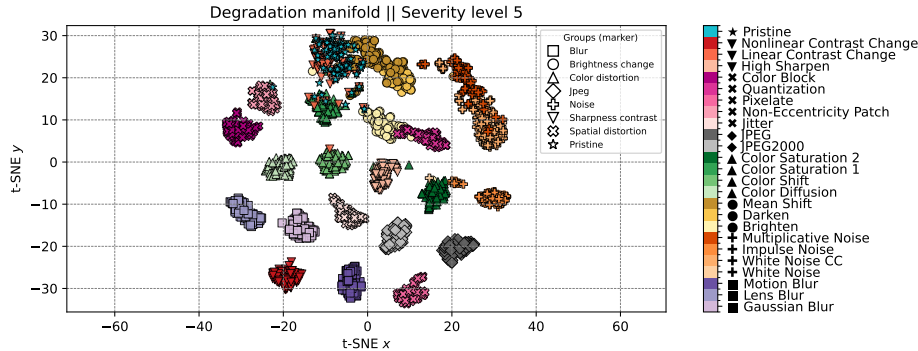
In Figure 4, severity level 5 samples from COCO are shown for different degradation families. Most degradation types form distinct clusters, demonstrating strong separability in embedding space. Degradations such as linear contrast changes or global intensity shifts appear closer to the pristine cluster, reflecting smaller geometric deviation. While this proximity aligns with the comparatively moderate mAP changes observed for these degradations (Figure 3), we emphasize that the embedding is optimized to capture degradation structure rather than task performance.

Pristine embeddings exhibit minor dispersion due to natural acquisition variability in COCO. Despite this, degraded samples form well-separated structures, confirming that the learned geometry captures systematic degradation beyond nominal data variation.

Figure 5 further illustrates semantic independence: pristine images from multiple datasets cluster together despite differences in scene content and acquisition conditions. BDD [55] and KITTI [13] were



(a) Degrations from Michaelis et al. [36] based on [17]



(b) Degrations from Agnolucci et al. [1]

Figure 4: t-SNE visualization [19] of the learned degradation manifold under two corruption taxonomies. **(Top)** Degrations from Michaelis et al. [36] based on [17]. **(Bottom)** Degrations from Agnolucci et al. [1]. Each color denotes a specific degradation type, while marker styles indicate the corresponding degradation group. For visualization, 100 COCO [28] samples are corrupted at severity level 5. Distinct clusters emerge for different degradation types. For training, only the deegrations from Agnolucci et al. [1] were used.

not part of the training pool, whereas the remaining datasets were. This suggests that the manifold generalizes across datasets and remains largely content-agnostic.

4.4.3 SELF-AWARENESS UNDER DEGRADATION

Table 1 reports AUROC for pristine vs. degraded separability on COCO under mixed corruptions across five severity levels. The proposed degradation manifold achieves the highest separability across detector backbones (up to 97.14 AUROC at severity 5 and above 88 at severity 1), and transfers across architectures (YOLOv9, YOLOv11, RT-DETR), indicating robustness to backbone choice.

Compared to probabilistic detector uncertainties, feature-density modeling, and IQA monitors, our method yields a substantial margin in AUROC across severities. These results suggest that explicitly structuring degradation geometry within task-aligned multi-layer representations yields a more reliable signal for degradation-induced covariate shift than output uncertainty or perceptual quality modeling alone.

IQA-based monitors provide moderate separability: score-based variants (e.g., CLIPIQA [50], MANIQA [54]) achieve AUROC in the ~ 53 – 70 range depending on severity. Embedding-based variants show a clear split: ARNIQA embeddings transfer well (up to 85.74 at severity 5), whereas CLIP-based IQA embeddings perform substantially worse, indicating embeddings dominated by semantic alignment rather than degradation geometry.

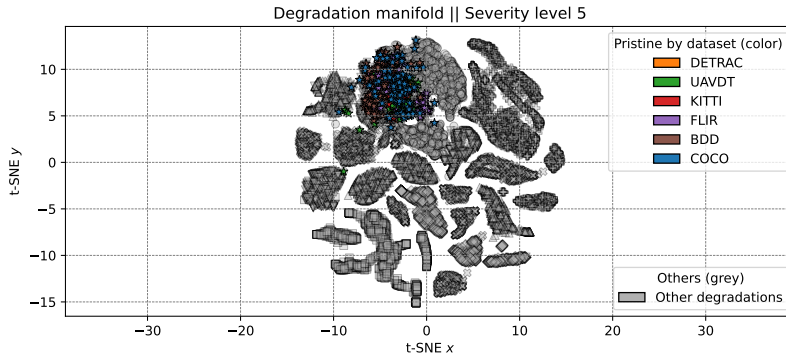


Figure 5: t-SNE visualization [19] of the learned degradation manifold. Samples are drawn from multiple datasets (COCO [28], BDD [55], KITTI [13], DETRAC [53], UAVDT [8], and FLIR (VIS) [11]). Degradations are clearly separated in embedding space, while pristine images form a compact cluster across datasets, indicating content-independence of the learned representation. Notably, BDD and KITTI images were not used during training, demonstrating cross-dataset generalization of the degradation manifold and that the embedding organizes images according to degradation characteristics rather than semantic content.

Detector-derived uncertainty depends strongly on scoring rule and aggregation statistic. Across nine probabilistic detector variants, the raw confidence score performs best among output-based signals (up to 77.65 at severity 5), but remains below the degradation manifold and relies on stable object hypotheses

Normalizing flows trained on pooled backbone features show limited separability at low severities and improve mainly under strong corruption; even multi-scale variants remain below 70 AUROC at severity 5, suggesting that density estimation on strongly pooled detector features struggles to capture fine-grained degradation structure.

Beyond the synthetic COCO benchmark, we evaluate the degradation manifold in (i) cross-dataset zero-shot transfer and (ii) natural weather-induced distribution shift.

Cross-Dataset Evaluation. The degradation manifold is trained on COCO [28] and evaluated without adaptation on several other datasets (KITTI [13], VISDRONE [61], DETRAC [53], UAVDT [8], and FLIR (VIS) [11]). The results are shown in Table 2. Despite substantial changes in scene layout, camera setup, and object scales, the manifold maintains strong pristine–degraded separability, indicating that it captures degradation structure rather than dataset-specific semantics.

Mixed-Dataset Evaluation. To further assess content-independence, we evaluate the degradation manifold under mixed-dataset conditions. In this setting, pristine images are sampled from a combination of datasets, while degraded images originate from the degraded counterpart of the same combined pool. To avoid dataset-imbalance effects, the number of COCO samples is subsampled to match the size of the secondary dataset in each pair.

This protocol introduces simultaneous variation in scene content, acquisition characteristics, and degradation severity. Importantly, the monitor is not trained to distinguish datasets, but to capture degradation-induced deviation from nominal imaging conditions.

As shown in Table 3, the degradation manifold maintains strong pristine–degraded separability across severity levels under mixed-dataset conditions. The consistently high AUROC indicates that the learned representation does not collapse under moderate semantic shift and remains primarily aligned with degradation structure rather than dataset identity.

Model	Severity levels AUROC \uparrow				
	1	2	3	4	5
Image Quality Assessment (IQA)					
MANIQA [54] (score-based)	52.88	54.49	55.27	56.67	61.56
MANIQA [54] (embedding-based; prototype anchored)	65.87	71.55	73.42	76.97	77.30
QualiCLIP [2] (score-based)	53.17	56.77	66.28	70.60	72.53
QualiCLIP [2] (embedding-based; prototype anchored)	45.36	41.53	46.77	49.79	56.16
QualiCLIP+ [2] (score-based)	52.56	57.90	65.49	69.18	70.87
QualiCLIP+ [2] (embedding-based; prototype anchored)	47.04	42.45	45.31	50.23	56.24
CLIQQA [50] (score-based)	57.78	60.43	62.29	69.28	69.71
CLIQQA [50] (embedding-based; prototype anchored)	49.36	47.71	47.58	46.65	45.76
CLIQQA+ [50] (score-based)	56.42	58.11	61.03	63.45	67.81
CLIQQA+ [50] (embedding-based; prototype anchored)	49.85	48.65	47.57	46.61	45.33
ARNIQUA [1] (score-based)	52.09	52.83	58.26	58.43	60.23
ARNIQUA [1] (embedding-based; prototype anchored)	73.60	80.07	80.58	83.30	85.74
Top-3 Detection Uncertainties ([41, 15])					
Trace (RetinaNet ES)	52.61	55.31	57.14	60.29	65.44
Trace (DETR NLL)	51.14	54.83	58.96	59.68	63.61
Determinant (RetinaNet NLL)	49.48	51.09	50.94	54.13	58.23
Determinant (RetinaNet ES)	49.65	50.57	51.29	52.66	56.39
Entropy (Regression) (RetinaNet ES)	52.73	55.15	57.67	60.82	66.51
Entropy (Regression) (FasterRCNN NLL)	51.65	51.66	55.72	56.90	64.87
Confidence Score (RetinaNet NLL)	52.91	56.93	61.51	69.69	77.65
Confidence Score (RetinaNet ES)	52.55	56.77	60.72	68.10	75.28
Entropy (Classification) (FasterRCNN ES)	54.70	59.97	62.84	68.47	77.60
Entropy (Classification) (FasterRCNN NLL)	53.31	59.65	64.35	70.43	77.33
Normalizing Flows (adapted from [33])					
NF <i>backbone</i> (C4, C5)	49.60	49.90	51.12	56.20	61.53
NF <i>backbone</i> (C1, C2, C3)	49.70	50.10	55.12	64.40	73.56
NF <i>backbone</i> (all; C1–C5)	49.80	50.20	56.12	64.90	73.45
M-NF <i>backbone</i> (C4, C5)	49.70	50.10	55.76	61.60	67.54
M-NF <i>backbone</i> (C1, C2, C3)	49.80	50.20	58.61	63.80	68.94
M-NF <i>backbone</i> (all; C1–C5)	49.90	50.25	58.76	63.90	69.12
Degradation Manifold DM (Ours)					
DM backbone YOLOv10-m	88.64	89.70	89.75	95.28	97.14
DM backbone RT DETR-l	83.88	88.29	90.37	95.61	97.11
DM backbone YOLOv9-m	87.64	89.06	90.07	95.66	96.62
DM backbone YOLOv11-m	85.84	89.12	89.95	94.58	96.04

Table 1: AUROC scores of detecting degradation-induced covariate shift for synthetically corrupted variants of the COCO dataset. Best results are highlighted as **first**, **second**, and **third**.

Degradation Manifold (Ours)					
Dataset	Severity levels AUROC \uparrow				
	1	2	3	4	5
VISDRONE [61]	83.66	89.15	92.08	95.85	96.79
KITTI [13]	94.19	96.37	97.16	97.25	98.52
DETRAC [53]	94.65	97.05	98.87	99.69	99.81
FLIR (VIS) [11]	82.83	91.39	92.72	95.11	96.66
UAVDT [8]	92.12	94.71	95.56	98.78	98.83

Table 2: AUROC scores of detecting OoD covariate shift using our degradation manifold across different datasets.

Natural Weather Shift. To assess real-world distribution shift, we evaluate on weather-affected subsets of Seeing Through Fog (STF) [4] and BDD [55]. For both datasets, weather metadata is used to construct an ID (nominal) vs. OoD (adverse weather) split. Since labels such as *wet road* may co-occur with rainy tags, we manually refine the split to ensure that the OoD partition contains images with clearly visible weather effects (details in Appendix 6). Results are summarized in Table 4. Compared to synthetic corruptions, separability under natural weather shift is weaker but remains clearly above chance. Training

Degradation Manifold (Ours)						
Datasets	Severity levels AUROC \uparrow					
	1	2	3	4	5	
COCO [28] & VISDRONE [61]	83.54	89.91	90.03	95.06	95.95	
COCO [28] & KITTI [13]	89.27	92.44	93.86	96.40	97.21	
COCO [28] & DETRAC [53]	92.26	93.29	94.92	98.62	98.97	
COCO [28] & FLIR (VIS) [11]	82.45	88.92	89.32	94.32	95.97	
COCO [28] & UAVDT [8]	89.77	92.12	92.39	97.51	98.21	

Table 3: AUROC for pristine–degraded separability under mixed-dataset evaluation. Pristine samples are drawn from combined datasets, while degraded samples originate from a degraded version of the datasets. COCO is subsampled for class-balanced comparison. Results demonstrate stable degradation-aware separability under simultaneous content and degradation variation.

with synthetic weather corruptions [17] improves AUROC consistently across **heavy snow**, **dense fog**, and **heavy rain**, indicating improved transfer to related real-world conditions.

Degradation Manifold (Ours)			
Dataset	Subset (OoD)	Weather aug. (train)	AUROC \uparrow
STF [4]	heavy snow	x	68.85
STF [4]	heavy snow	\checkmark	71.94
STF [4]	dense fog	x	77.37
STF [4]	dense fog	\checkmark	81.50
STF [4]	heavy rain	x	78.84
STF [4]	heavy rain	\checkmark	86.66
BDD [55]	heavy rain	x	64.96
BDD [55]	heavy rain	\checkmark	88.52

Table 4: Natural weather-induced distribution shifts on BDD [55] and STF [4]. AUROC measures separability between nominal-weather (pristine) (ID) and adverse-weather (OoD) subsets. Training with synthetic weather corruptions improves transfer to real-world heavy weather conditions.

Ablation Study. Table 5 analyzes the impact of multi-layer readout, attention-based pooling, and hard negative mining using a YOLOv10-m backbone. The full configuration consistently achieves the strongest separability.

Degradation Manifold (Ours)					
Variant	Severity levels AUROC \uparrow				
	1	2	3	4	5
Full model (multi-layer + attention + hard neg.)	88.64	89.70	89.75	95.28	97.14
Last backbone layer only	81.87	85.13	87.56	89.13	92.75
Global average pooling (no attention)	85.51	88.44	89.49	95.01	96.30
Without hard negative mining	86.00	87.17	87.58	90.41	91.54

Table 5: Ablation study of the proposed degradation manifold using a YOLOv10-m backbone. We analyze the impact of multi-layer readout, attention-based pooling, and hard negative mining on AUROC across severity levels. The full configuration consistently achieves the strongest separability.

Single-Degradation Analysis. For fine-grained characterization, we report per-corruption AUROC across severity levels in Appendix (Tables 8 and 7). Although the manifold is trained using IQA-style degradations [1], it exhibits consistent severity ordering on robustness corruptions [17]: separability increases monotonically with corruption strength for most degradation types. This indicates that the embedding captures structured degradation geometry beyond the exact transformations observed during training.

5. Discussion and Limitations

Data-side Self-Awareness. We formulate self-awareness through an explicit *data-side* degradation term (Eq. 1) that separates prediction confidence from input fidelity. The learned score $S_{\text{deg}}(\mathbf{x})$ is not intended as a calibrated predictor of task failure, but as an operational warning signal indicating deviation from nominal imaging conditions. This indirect formulation is deliberate: in realistic deployments, exhaustive supervision of failure cases under distribution shift is typically unavailable. Accordingly, we evaluate monitors by pristine–degraded separability (AUROC) and report detection performance only for context. The monitor is intended as a gating mechanism that flags potentially unsafe operating regimes rather than replacing task-level evaluation.

The learned degradation manifold exhibits strong separability across severity levels and clear clustering by degradation type. This structure enables flexible operating points: the monitor can be tuned to trigger warnings only for high-severity deviations while ignoring mild shifts. Because the embedding space is organized by degradation regime, the inferred regime identity could additionally support targeted downstream responses (e.g., requesting higher-quality input, adapting preprocessing, or switching to a more robust model variant). Thus, even without directly predicting mAP, reliable separation provides actionable system-level information.

Alternative Monitors. Signals derived from detector outputs (confidence, entropy, covariance statistics) reflect prediction uncertainty rather than input fidelity. They depend on the presence and stability of object hypotheses and implicitly assume meaningful detections in the scene. Under strong degradations, detections may disappear or become unstable, limiting the reliability of image-level aggregation. Performance further depends strongly on the training objective (ES, NLL, DMM), with *energy score* variants yielding more balanced behavior. Although raw confidence achieves the strongest AUROC among detector-based signals, it remains clearly below the proposed manifold and inherits the fundamental assumption of object presence.

Normalizing-flow baselines aim to model feature likelihood under nominal conditions. However, density estimation in high-dimensional detector feature spaces at realistic resolutions typically requires strong compression (e.g., global pooling), which limits expressiveness. Moreover, likelihood models are known to exhibit counterintuitive behavior under distribution shift [40, 25]. In contrast, our approach shapes representation geometry directly through contrastive learning and avoids explicit density modeling, yielding more stable separability and better transfer across datasets.

Modern no-reference IQA models provide a meaningful comparison because they learn degradation-sensitive representations. In our setting, however, they are repurposed as zero-shot monitors on detection-style data. We evaluate both their predicted quality scores and prototype-anchored embedding distances. Empirically, ARNIQA embeddings transfer well, whereas CLIP-based IQA embeddings perform substantially weaker, indicating that semantic alignment objectives do not necessarily yield geometrically stable degradation representations. While IQA scores provide reasonable separability, the proposed detector-aligned multi-layer manifold consistently performs better.

Limitations and Outlook. The proposed manifold measures deviation from nominal imaging conditions but does not directly estimate task correctness. As with other shift monitors, degradation distance cannot guarantee performance degradation on a per-instance basis: some images may be degraded yet still detectable, while others may fail for semantic or contextual reasons despite being visually clean. In addition, our degradation sampling focuses on image formation effects (noise, blur, compression, resolution and related distortions) and does not explicitly cover semantic distribution shifts, domain changes, or label noise. Finally, the choice of multi-layer readout, pooling operator, and hard-negative construction impacts the resulting geometry. While our ablations validate key design choices, more principled fusion strategies may further improve robustness under complex mixed degradations.

6. Conclusion

We presented a degradation-aware framework for self-aware object detection that explicitly structures detector representations according to image fidelity. By jointly optimizing selected backbone layers with a lightweight contrastive embedding head, we learn a *degradation manifold* that organizes images by degradation type and severity rather than semantic content.

The resulting representation enables intrinsic, image-level reliability estimation via geometric distance to a pristine reference prototype, without requiring degradation labels, explicit density modeling, or post-hoc uncertainty aggregation. In this formulation, self-awareness emerges directly from the detector’s feature geometry.

Across synthetic corruptions, cross-dataset transfer, and natural weather shifts, the proposed manifold consistently yields strong pristine–degraded separability and typically outperforms detector-derived uncertainty, feature-density modeling, and modern IQA baselines.

We view degradation-aware representation geometry as a promising and practical, detector-agnostic foundation for self-aware perception systems operating under real-world visual variability.

References

- [1] Lorenzo Agnolucci, Leonardo Galteri, Marco Bertini, and Alberto Del Bimbo. Arnika: Learning distortion manifold for image quality assessment. In *Proceedings of the IEEE/CVF Winter Conference on Applications of Computer Vision*, pages 189–198, 2024.
- [2] Lorenzo Agnolucci, Leonardo Galteri, and Marco Bertini. Quality-aware image-text alignment for opinion-unaware image quality assessment, 2025. URL <https://arxiv.org/abs/2403.11176>.
- [3] Simone Bianco, Luigi Celona, and Paolo Napoletano. Disentangling image distortions in deep feature space. *Pattern Recognition Letters*, 148:128–135, 2021. ISSN 0167-8655. doi: <https://doi.org/10.1016/j.patrec.2021.05.008>. URL <https://www.sciencedirect.com/science/article/pii/S0167865521001859>.
- [4] Mario Bijelic, Tobias Gruber, Fahim Mannan, Florian Kraus, Werner Ritter, Klaus Dietmayer, and Felix Heide. Seeing through fog without seeing fog: Deep multimodal sensor fusion in unseen adverse weather. In *The IEEE Conference on Computer Vision and Pattern Recognition (CVPR)*, June 2020.
- [5] Ting Chen, Simon Kornblith, Mohammad Norouzi, and Geoffrey Hinton. A simple framework for contrastive learning of visual representations. In *International conference on machine learning*, pages 1597–1607. PMLR, 2020.
- [6] Chih-Hong Cheng. Provably-robust runtime monitoring of neuron activation patterns. In *Design, Automation and Test in Europe Conference and Exhibition (DATE)*, pages 1310–1313, 2021. doi: 10.23919/DATE51398.2021.9473957.
- [7] Laurent Dinh, Jascha Sohl-Dickstein, and Samy Bengio. Density estimation using real NVP. In *5th International Conference on Learning Representations, ICLR 2017, Toulon, France, April 24-26, 2017, Conference Track Proceedings*. OpenReview.net, 2017. URL <https://openreview.net/forum?id=HkpbhH91x>.
- [8] Dawei Du, Yuankai Qi, Hongyang Yu, Yi-Fan Yang, Kaiwen Duan, Guorong Li, Weigang Zhang, Qingming Huang, and Qi Tian. The unmanned aerial vehicle benchmark: Object detection and tracking. In Vittorio Ferrari, Martial Hebert, Cristian Sminchisescu, and Yair Weiss, editors, *Computer Vision - ECCV 2018 - 15th European Conference, Munich, Germany, September 8-14, 2018, Proceedings, Part X*, volume 11214 of *Lecture Notes in Computer Science*, pages 375–391. Springer, 2018. doi: 10.1007/978-3-030-01249-6_23. URL https://doi.org/10.1007/978-3-030-01249-6_23.
- [9] Xuefeng Du, Zhaoning Wang, Mu Cai, and Sharon Li. Vos: Learning what you don’t know by virtual outlier synthesis. In *International Conference on Learning Representations*, 2022. URL <https://openreview.net/forum?id=TW7d65uYu5M>.
- [10] Di Feng, Lars Rosenbaum, Claudius Glaeser, Fabian Timm, and Klaus Dietmayer. Can we trust you? on calibration of a probabilistic object detector for autonomous driving. *The IEEE/RSJ International Conference on Intelligent Robots and Systems (IROS)*, 2020.
- [11] FLIR (V2). Free flir thermal dataset for algorithm training. 2022. Available at <https://www.flir.com/oem/adas/dataset/european-regional-thermal-dataset/>.
- [12] Yarín Gal and Zoubin Ghahramani. Dropout as a bayesian approximation: Representing model uncertainty in deep learning. In Maria Florina Balcan and Kilian Q. Weinberger, editors, *Proceedings of The 33rd International Conference on Machine Learning*, volume 48 of *Proceedings of Machine Learning Research*, pages 1050–1059, New York, New York, USA, 20–22 Jun 2016. PMLR. URL <https://proceedings.mlr.press/v48/gal16.html>.
- [13] Andreas Geiger, Philip Lenz, and Raquel Urtasun. Are we ready for autonomous driving? the KITTI Vision Benchmark Suite. In *Conference on Computer Vision and Pattern Recognition (CVPR)*, 2012.
- [14] Tilmann Gneiting and Adrian E Raftery. Strictly proper scoring rules, prediction, and estimation. *Journal of the American Statistical Association*, 102(477):359–378, 2007. doi: 10.1198/

016214506000001437. URL <https://doi.org/10.1198/016214506000001437>.
- [15] Ali Harakeh and Steven L. Waslander. Estimating and evaluating regression predictive uncertainty in deep object detectors. In *International Conference on Learning Representations*, 2021. URL <https://openreview.net/forum?id=YLewtnvKgR7>.
- [16] Kaiming He, Xiangyu Zhang, Shaoqing Ren, and Jian Sun. Deep residual learning for image recognition. In *Proceedings of the IEEE conference on computer vision and pattern recognition*, pages 770–778, 2016.
- [17] Dan Hendrycks and Thomas Dietterich. Benchmarking neural network robustness to common corruptions and perturbations. In *International Conference on Learning Representations*, 2019. URL <https://openreview.net/forum?id=HJz6tiCqYm>.
- [18] Dan Hendrycks and Kevin Gimpel. A baseline for detecting misclassified and out-of-distribution examples in neural networks. In *International Conference on Learning Representations*, 2017. URL <https://openreview.net/forum?id=Hkg4TI9xl>.
- [19] Geoffrey Hinton and Sam Roweis. Stochastic neighbor embedding. *Advances in neural information processing systems*, 15:833–840, 2003. URL <http://citeseerx.ist.psu.edu/viewdoc/download?doi=10.1.1.13.7959&rep=rep1&type=pdf>.
- [20] Rui Huang, Andrew Geng, and Yixuan Li. On the importance of gradients for detecting distributional shifts in the wild. In *Proceedings of the 35th International Conference on Neural Information Processing Systems, NIPS '21*, Red Hook, NY, USA, 2021. Curran Associates Inc. ISBN 9781713845393.
- [21] Glenn Jocher and Jing Qiu. Ultralytics YOLO11, 2024. URL <https://github.com/ultralytics/ultralytics>.
- [22] Daniel Kang, Deepti Raghavan, Peter Bailis, and Matei Zaharia. Model assertions for monitoring and improving ml models. In I. Dhillon, D. Papailiopoulos, and V. Sze, editors, *Proceedings of Machine Learning and Systems*, volume 2, pages 481–496, 2020.
- [23] Alex Kendall and Yarin Gal. What uncertainties do we need in bayesian deep learning for computer vision? In I. Guyon, U. V. Luxburg, S. Bengio, H. Wallach, R. Fergus, S. Vishwanathan, and R. Garnett, editors, *Advances in Neural Information Processing Systems 30*, pages 5574–5584. Curran Associates, Inc., 2017.
- [24] Diederik P. Kingma and Max Welling. Auto-encoding variational bayes. In Yoshua Bengio and Yann LeCun, editors, *International Conference on Learning Representations (ICLR)*.
- [25] Polina Kirichenko, Pavel Izmailov, and Andrew G Wilson. Why normalizing flows fail to detect out-of-distribution data. In H. Larochelle, M. Ranzato, R. Hadsell, M.F. Balcan, and H. Lin, editors, *Advances in Neural Information Processing Systems*, volume 33, pages 20578–20589. Curran Associates, Inc., 2020. URL https://proceedings.neurips.cc/paper_files/paper/2020/file/ecb9fe2fbb99c31f567e9823e884dbec-Paper.pdf.
- [26] Ivan Kobyzev, Simon J.D. Prince, and Marcus A. Brubaker. Normalizing flows: An introduction and review of current methods. *IEEE Transactions on Pattern Analysis and Machine Intelligence*, 43(11): 3964–3979, 2021. doi: 10.1109/TPAMI.2020.2992934.
- [27] Shiyu Liang, Yixuan Li, and R. Srikant. Enhancing the reliability of out-of-distribution image detection in neural networks. In *International Conference on Learning Representations*, 2018. URL <https://openreview.net/forum?id=H1VGkIxRZ>.
- [28] Tsung-Yi Lin, Michael Maire, Serge Belongie, James Hays, Pietro Perona, Deva Ramanan, Piotr Dollár, and C Lawrence Zitnick. Microsoft coco: Common objects in context. In *European conference on computer vision (ECCV)*, pages 740–755. Springer, 2014.
- [29] Jiawei Liu, Zhijie Wang, Lei Ma, Chunrong Fang, Tongtong Bai, Xufan Zhang, Jia Liu, and Zhenyu Chen. Benchmarking object detection robustness against real-world corruptions. *International Journal*

of *Computer Vision*, 132(10):4398–4416, Oct 2024. ISSN 1573-1405. doi: 10.1007/s11263-024-02096-6. URL <https://doi.org/10.1007/s11263-024-02096-6>.

- [30] Weitang Liu, Xiaoyun Wang, John Owens, and Yixuan Li. Energy-based out-of-distribution detection. In H. Larochelle, M. Ranzato, R. Hadsell, M.F. Balcan, and H. Lin, editors, *Advances in Neural Information Processing Systems*, volume 33, pages 21464–21475. Curran Associates, Inc., 2020. URL https://proceedings.neurips.cc/paper_files/paper/2020/file/f5496252609c43eb8a3d147ab9b9c006-Paper.pdf.
- [31] Zhuang Liu and Kaiming He. A decade’s battle on dataset bias: Are we there yet? In *The Thirteenth International Conference on Learning Representations*, 2025. URL <https://openreview.net/forum?id=SctfBCLmWo>.
- [32] Dariush Lotfi, Mohammad-Ali Nikouei Mahani, Mohamad Koochi-Moghadam, and Kyongtae Ty Bae. Enhancing out-of-distribution detection in medical imaging with normalizing flows, 2025. URL <https://arxiv.org/abs/2502.11638>.
- [33] Dariush Lotfi, Mohammad-Ali Nikouei Mahani, Mohamad Koochi-Moghadam, and Kyongtae Ty Bae. Safeguarding ai in medical imaging: Post-hoc out-of-distribution detection with normalizing flows. *arXiv preprint arXiv:2502.11638*, 2025.
- [34] David J. C. MacKay. A practical bayesian framework for backpropagation networks. *Neural Computation*, 4(3):448–472, 1992. doi: 10.1162/neco.1992.4.3.448.
- [35] Thomas Mensink, Jakob Verbeek, Florent Perronnin, and Gabriela Csurka. Distance-based image classification: Generalizing to new classes at near-zero cost. *IEEE Transactions on Pattern Analysis and Machine Intelligence*, 35(11):2624–2637, 2013. doi: 10.1109/TPAMI.2013.83.
- [36] Claudio Michaelis, Benjamin Mitzkus, Robert Geirhos, Evgenia Rusak, Oliver Bringmann, Alexander S. Ecker, Matthias Bethge, and Wieland Brendel. Benchmarking robustness in object detection: Autonomous driving when winter is coming. In *Machine Learning for Autonomous Driving (NeurIPS Workshop)*, 2019.
- [37] Anish Mittal, Anush K. Moorthy, and Alan Conrad Bovik. No-reference image quality assessment in the spatial domain. *IEEE Transactions on Image Processing*, 21:4695–4708, 2012. URL <https://api.semanticscholar.org/CorpusID:2927709>.
- [38] Anish Mittal, Rajiv Soundararajan, and Alan C. Bovik. Making a “completely blind” image quality analyzer. *IEEE Signal Processing Letters*, 20(3):209–212, 2013. doi: 10.1109/LSP.2012.2227726.
- [39] Kevin P. Murphy. *Probabilistic Machine Learning: An introduction*. MIT Press, 2022. URL probml.ai.
- [40] Eric Nalisnick, Akihiro Matsukawa, Yee Whye Teh, Dilan Gorur, and Balaji Lakshminarayanan. Do deep generative models know what they don’t know? In *International Conference on Learning Representations*, 2019. URL <https://openreview.net/forum?id=H1xwNhCcYm>.
- [41] Kemal Oksuz, Tom Joy, and Puneet K. Dokania. Towards building self-aware object detectors via reliable uncertainty quantification and calibration. In *Conference on Computer Vision and Pattern Recognition (CVPR)*, 2023.
- [42] Yaniv Ovadia, Emily Fertig, Jie Ren, Zachary Nado, D. Sculley, Sebastian Nowozin, Joshua V. Dillon, Balaji Lakshminarayanan, and Jasper Snoek. *Can you trust your model’s uncertainty? evaluating predictive uncertainty under dataset shift*. Curran Associates Inc., Red Hook, NY, USA, 2019.
- [43] Joaquin Quionero-Candela, Masashi Sugiyama, Anton Schwaighofer, and Neil D. Lawrence. *Dataset Shift in Machine Learning*. The MIT Press, 2009. ISBN 0262170051.
- [44] Nermin Samet, Samet Hicsonmez, and Emre Akbas. Houghnet: Integrating near and long-range evidence for bottom-up object detection. In *European Conference on Computer Vision (ECCV)*, 2020.

- [45] Jake Snell, Kevin Swersky, and Richard Zemel. Prototypical networks for few-shot learning. In *Proceedings of the 31st International Conference on Neural Information Processing Systems, NIPS'17*, page 4080–4090, Red Hook, NY, USA, 2017. Curran Associates Inc. ISBN 9781510860964.
- [46] Yiyu Sun, Chuan Guo, and Yixuan Li. React: Out-of-distribution detection with rectified activations. In *Advances in Neural Information Processing Systems*, 2021.
- [47] Christiaan Viviers, Amaan Valiuddin, Francisco Caetano, Lemar Abdi, Lena Filatova, Peter de With, and Fons van der Sommen. Can your generative model detect out-of-distribution covariate shift? In *European Conference on Computer Vision (ECCV) Workshops*, 2024.
- [48] Ao Wang, Hui Chen, Lihao Liu, Kai CHEN, Zijia Lin, Jungong Han, and Guiguang Ding. YOLOv10: Real-time end-to-end object detection. In *The Thirty-eighth Annual Conference on Neural Information Processing Systems*, 2024. URL <https://openreview.net/forum?id=tz83Nyb711>.
- [49] Chien-Yao Wang, I-Hau Yeh, and Hong-Yuan Mark Liao. Yolov9: Learning what you want to learn using programmable gradient information. In *European Conference on Computer Vision (ECCV)*, pages 1–21, Cham, 2024. Springer Nature Switzerland.
- [50] Jianyi Wang, Kelvin C.K. Chan, and Chen Change Loy. Exploring clip for assessing the look and feel of images. In *Proceedings of the Thirty-Seventh AAAI Conference on Artificial Intelligence and Thirty-Fifth Conference on Innovative Applications of Artificial Intelligence and Thirteenth Symposium on Educational Advances in Artificial Intelligence, AAAI'23/IAAI'23/EAAI'23*. AAAI Press, 2023. ISBN 978-1-57735-880-0. doi: 10.1609/aaai.v37i2.25353. URL <https://doi.org/10.1609/aaai.v37i2.25353>.
- [51] Xiaohong Wang, Yunjie Pang, and Xiangcai Ma. Real distorted images quality assessment based on multi-layer visual perception mechanism and high-level semantics. *Multimedia Tools Appl.*, 79(35–36): 25905–25920, 2020. ISSN 1380-7501. doi: 10.1007/s11042-020-09222-9. URL <https://doi.org/10.1007/s11042-020-09222-9>.
- [52] Zhou Wang, A.C. Bovik, H.R. Sheikh, and E.P. Simoncelli. Image quality assessment: from error visibility to structural similarity. *IEEE Transactions on Image Processing*, 13(4):600–612, 2004. doi: 10.1109/TIP.2003.819861.
- [53] Longyin Wen, Dawei Du, Zhaowei Cai, Zhen Lei, Ming-Ching Chang, Honggang Qi, Jongwoo Lim, Ming-Hsuan Yang, and Siwei Lyu. UA-DETRAC: A new benchmark and protocol for multi-object detection and tracking. *Computer Vision and Image Understanding*, 2020.
- [54] Sidi Yang, Tianhe Wu, Shuwei Shi, Shanshan Lao, Yuan Gong, Mingdeng Cao, Jiahao Wang, and Yujiu Yang. Maniqa: Multi-dimension attention network for no-reference image quality assessment. In *Proceedings of the IEEE/CVF Conference on Computer Vision and Pattern Recognition*, pages 1191–1200, 2022.
- [55] Fisher Yu, Haofeng Chen, Xin Wang, Wenqi Xian, Yingying Chen, Fangchen Liu, Vashisht Madhavan, and Trevor Darrell. Bdd100k: A diverse driving dataset for heterogeneous multitask learning. In *IEEE/CVF Conference on Computer Vision and Pattern Recognition (CVPR)*, June 2020.
- [56] Kai Zhang, Jingyun Liang, Luc Van Gool, and Radu Timofte. Designing a practical degradation model for deep blind image super-resolution. In *Proceedings of the IEEE/CVF International Conference on Computer Vision*, pages 4791–4800, 2021.
- [57] Lily H. Zhang, Mark Goldstein, and Rajesh Ranganath. Understanding failures in out-of-distribution detection with deep generative models. *Proceedings of machine learning research*, 139:12427–12436, 2021. URL <https://api.semanticscholar.org/CorpusID:235826027>.
- [58] Lin Zhang, Lei Zhang, Xuanqin Mou, and David Zhang. Fsim: A feature similarity index for image quality assessment. *IEEE Transactions on Image Processing*, 20(8):2378–2386, 2011. doi: 10.1109/TIP.2011.2109730.

- [59] Wenlong Zhang, Guangyuan Shi, Yihao Liu, Chao Dong, and Xiao-Ming Wu. A closer look at blind super-resolution: Degradation models, baselines, and performance upper bounds. In *Proceedings of the IEEE/CVF Conference on Computer Vision and Pattern Recognition*, pages 527–536, 2022.
- [60] Yian Zhao, Wenyu Lv, Shangliang Xu, Jinman Wei, Guanzhong Wang, Qingqing Dang, Yi Liu, and Jie Chen. DETRs Beat YOLOs on Real-time Object Detection. In *Proceedings of the IEEE/CVF Conference on Computer Vision and Pattern Recognition (CVPR)*, pages 16965–16974, June 2024.
- [61] Pengfei Zhu, Longyin Wen, Dawei Du, Xiao Bian, Heng Fan, Qinghua Hu, and Haibin Ling. Detection and tracking meet drones challenge. *IEEE Transactions on Pattern Analysis and Machine Intelligence*, 44(11):7380–7399, 2021.

Supplementary Material

This Appendix provides supplementary information supporting our main paper. It includes expanded experimental details, additional results, and model configurations.

Detectors

To assess detector independence, we consider multiple current detection models as source for reading out feature maps to recognize distributional shift and to evaluate detection performance under the same degradation settings. These are:

YOLOv9. YOLOv9 [49] is a one-stage detector that revisits information preservation in deep architectures. It introduces *Programmable Gradient Information* (PGI), an auxiliary supervision scheme with additional training branches designed to mitigate error accumulation as network depth increases. YOLOv9 further proposes the *Generalized Efficient Layer Aggregation Network* (GELAN), a flexible backbone that supports different computational blocks while maintaining efficiency.

YOLOv10. YOLOv10 [48] is a one-stage detector that removes the need for non-maximum suppression (NMS) at inference. This is achieved via *consistent dual assignments* during training, implemented through paired one-to-many and one-to-one matching along with an additional one-to-one detection head. Both heads are optimized jointly to provide richer supervision while enabling NMS-free inference. Results are shown in Figure 3.

YOLOv11. YOLOv11 [21] is a recent YOLO-family variant that introduces incremental architectural changes aimed at improving the speed-accuracy trade-off. Compared to prior Ultralytics models, it uses updated building blocks (e.g., C3k2) and integrates attention-style modules (e.g., C2PSA), while retaining standard multi-scale aggregation components such as SPPF.

RT-DETR. RT-DETR [60] is an end-to-end transformer-based detector that, like other DETR variants, performs set prediction and is therefore NMS-free by design. To reduce the computational cost typical of DETR-style models, RT-DETR employs a hybrid encoder for multi-scale feature processing and uses a query-selection strategy to initialize decoder queries more effectively.

We use the Ultralytics [21] implementations¹ with COCO (train2017) pretrained weights and default settings, including an input size of 640. To standardize score filtering across detectors for detection performance evaluation, we set the confidence threshold to 0.001 for all runs.

The full (*backbone* and *head*) layers from RT-DETR-l are listed in Listing 1. For feature map extraction, the layers [0, 2, 4, 8, 9] are used.

For YOLOv9-m, the key *backbone* and *head* layers are presented in Listing 2. For feature map extraction, the layers [0, 1, 3, 5, 7, 9] are used.

The primary *backbone* and *head* layers for YOLOv10-m are shown in Listing 3. Layers used are [0, 1, 3, 5, 7, 10].

For YOLOv11, the selected layers or building blocks used for activation extraction are presented in Listing 4. Layers used are [0, 1, 3, 5, 7, 10]

1. <https://github.com/ultralytics/ultralytics> (accessed 18.02.2026)

Listing 1: RT-DETR-l *backbone* and *head* layers ([configuration file](#); last accessed February 2026).

```

backbone:
# [from, repeats, module, args]
- [-1, 1, HGStem, [32, 48]] # 0-P2/4
- [-1, 6, HGBlock, [48, 128, 3]] # stage 1
- [-1, 1, DWConv, [128, 3, 2, 1, False]] # 2-P3/8
- [-1, 6, HGBlock, [96, 512, 3]] # stage 2
- [-1, 1, DWConv, [512, 3, 2, 1, False]] # 4-P3/16
- [-1, 6, HGBlock, [192, 1024, 5, True, False]] # 5
- [-1, 6, HGBlock, [192, 1024, 5, True, True]] # 6
- [-1, 6, HGBlock, [192, 1024, 5, True, True]] # 7
- [-1, 1, DWConv, [1024, 3, 2, 1, False]] # 8-P4/32
- [-1, 6, HGBlock, [384, 2048, 5, True, False]] # 9
head:
- [-1, 1, Conv, [256, 1, 1, None, 1, 1, False]] # 10
- [-1, 1, AIFI, [1024, 8]] #11
- [-1, 1, Conv, [256, 1, 1]] # 12,
- [-1, 1, nn.Upsample, [None, 2, "nearest"]] #13
- [7, 1, Conv, [256, 1, 1, None, 1, 1, False]] # 14
- [[-2, -1], 1, Concat, [1]] # 15
- [-1, 3, RepC3, [256]] # 16
- [-1, 1, Conv, [256, 1, 1]] # 17
- [-1, 1, nn.Upsample, [None, 2, "nearest"]] # 18
- [3, 1, Conv, [256, 1, 1, None, 1, 1, False]] # 19
- [[-2, -1], 1, Concat, [1]] # 20
- [-1, 3, RepC3, [256]] # 21
- [-1, 1, Conv, [256, 3, 2]] # 22,
- [[-1, 17], 1, Concat, [1]] # 23
- [-1, 3, RepC3, [256]] # 24
- [-1, 1, Conv, [256, 3, 2]] # 25
- [[-1, 12], 1, Concat, [1]] # 26
- [-1, 3, RepC3, [256]] # 27

```

Listing 2: YOLOv9-m *backbone* and *head* layers ([configuration file](#); last accessed February 2026).

```

backbone:
- [-1, 1, Conv, [32, 3, 2]] # 0-P1/2
- [-1, 1, Conv, [64, 3, 2]] # 1-P2/4
- [-1, 1, RepNCSPPELAN4, [128, 128, 64, 1]] # 2
- [-1, 1, AConv, [240]] # 3-P3/8
- [-1, 1, RepNCSPPELAN4, [240, 240, 120, 1]] # 4
- [-1, 1, AConv, [360]] # 5-P4/16
- [-1, 1, RepNCSPPELAN4, [360, 360, 180, 1]] # 6
- [-1, 1, AConv, [480]] # 7-P5/32
- [-1, 1, RepNCSPPELAN4, [480, 480, 240, 1]] # 8
- [-1, 1, SPPELAN, [480, 240]] # 9
head:
- [-1, 1, nn.Upsample, [None, 2, "nearest"]] # 10
- [[-1, 6], 1, Concat, [1]] # 11
- [-1, 1, RepNCSPPELAN4, [360, 360, 180, 1]] # 12
- [-1, 1, nn.Upsample, [None, 2, "nearest"]] #13
- [[-1, 4], 1, Concat, [1]] # 14
- [-1, 1, RepNCSPPELAN4, [240, 240, 120, 1]] # 15
- [-1, 1, AConv, [180]] #16
- [[-1, 12], 1, Concat, [1]] # 17
- [-1, 1, RepNCSPPELAN4, [360, 360, 180, 1]] # 18 (P4/16-medium)
- [-1, 1, AConv, [240]] # 19
- [[-1, 9], 1, Concat, [1]] # 20
- [-1, 1, RepNCSPPELAN4, [480, 480, 240, 1]] # 21 (P5/32-large)

```

Listing 3: YOLOv10-m *backbone* and *head* layers ([configuration file](#); last accessed February 2026)

```

backbone:
# [from, repeats, module, args]
- [-1, 1, Conv, [64, 3, 2]] # 0-P1/2
- [-1, 1, Conv, [128, 3, 2]] # 1-P2/4
- [-1, 3, C2f, [128, True]] # 4
- [-1, 1, Conv, [256, 3, 2]] # 3-P3/8
- [-1, 6, C2f, [256, True]] # 4
- [-1, 1, SCDwn, [512, 3, 2]] # 5-P4/16
- [-1, 6, C2f, [512, True]] # 6
- [-1, 1, SCDwn, [1024, 3, 2]] # 7-P5/32
- [-1, 3, C2fCIB, [1024, True]]
- [-1, 1, SPPF, [1024, 5]] # 9
- [-1, 1, PSA, [1024]] # 10
head:
- [-1, 1, nn.Upsample, [None, 2, "nearest"]] # 11
- [[-1, 6], 1, Concat, [1]] # 12 P4
- [-1, 3, C2f, [512]] # 13
- [-1, 1, nn.Upsample, [None, 2, "nearest"]] # 14
- [[-1, 4], 1, Concat, [1]] # 15 P3
- [-1, 3, C2f, [256]] # 16 (P3/8-small)
- [-1, 1, Conv, [256, 3, 2]] # 17
- [[-1, 13], 1, Concat, [1]] # 18
- [-1, 3, C2fCIB, [512, True]] # 19 (P4/16-medium)
- [-1, 1, SCDwn, [512, 3, 2]] # 20
- [[-1, 10], 1, Concat, [1]] # 21
- [-1, 3, C2fCIB, [1024, True]] # 22 (P5/32-large)

```

Listing 4: YOLOv11 *backbone* and *head* layers ([configuration file](#); last accessed February 2026).

```

backbone:
# [from, repeats, module, args]
- [-1, 1, Conv, [64, 3, 2]] # 0-P1/2
- [-1, 1, Conv, [128, 3, 2]] # 1-P2/4
- [-1, 2, C3k2, [256, False, 0.25]]
- [-1, 1, Conv, [256, 3, 2]] # 3-P3/8
- [-1, 2, C3k2, [512, False, 0.25]]
- [-1, 1, Conv, [512, 3, 2]] # 5-P4/16
- [-1, 2, C3k2, [512, True]] # 6
- [-1, 1, Conv, [1024, 3, 2]] # 7-P5/32
- [-1, 2, C3k2, [1024, True]]
- [-1, 1, SPPF, [1024, 5]] # 9
- [-1, 2, C2PSA, [1024]] # 10
head:
- [-1, 1, nn.Upsample, [None, 2, "nearest"]] # 11
- [[-1, 6], 1, Concat, [1]] # 12
- [-1, 2, C3k2, [512, False]] # 13
- [-1, 1, nn.Upsample, [None, 2, "nearest"]] # 14
- [[-1, 4], 1, Concat, [1]] # 15
- [-1, 2, C3k2, [256, False]] # 16 (P3/8-small)
- [-1, 1, Conv, [256, 3, 2]] # 17
- [[-1, 13], 1, Concat, [1]] # 18
- [-1, 2, C3k2, [512, False]] # 19 (P4/16-medium)
- [-1, 1, Conv, [512, 3, 2]] # 20
- [[-1, 10], 1, Concat, [1]] # 21
- [-1, 2, C3k2, [1024, True]] # 22 (P5/32-large)

```

Datasets

To evaluate self-awareness under *natural* distribution shift, we construct weather-based ID/OoD splits on Seeing Through Fog (STF) [4] and BDD100K [55]. In both cases, the *in-distribution (ID)* partition corresponds to nominal/clear-weather conditions, while the *out-of-distribution (OoD)* partition contains images with *strong, visually apparent* adverse weather.

STF provides weather annotations that include *Dense Fog* and *Heavy Snow*. We define ID as clear/nominal conditions and construct two OoD subsets using the corresponding labels (*Dense Fog* and *Heavy Snow*). For the *Rain* condition, we further filter the labeled subset by visual inspection to reduce ambiguous samples (e.g., scenes primarily characterized by wet surfaces without clearly visible precipitation), ensuring that the OoD split reflects a perceptually strong weather shift rather than subtle appearance changes.

BDD100K includes attribute metadata such as *weather* (e.g., **clear**, **rainy**). We define ID using the **clear** subset and define OoD using the **rainy** subset. However, the **rainy** label can include scenes with weak or ambiguous cues (e.g., *wet road* without visible rain). To obtain a conservative OoD split, we manually exclude such ambiguous samples and retain only images with strong visible weather effects (e.g., rain streaks, reduced visibility, windshield artifacts). This refinement increases the semantic consistency of the OoD partition and avoids inflating OoD size with near-ID conditions.

Natural weather shift is inherently heterogeneous and entangled with scene content and acquisition conditions. Our manual refinement is therefore intentionally conservative: it aims to create an OoD subset that corresponds to *clearly adverse* conditions, yielding a cleaner evaluation of whether the monitor separates nominal from strongly shifted inputs. Example images from the resulting ID/OoD splits are shown in Figure 6 and Figure 7.

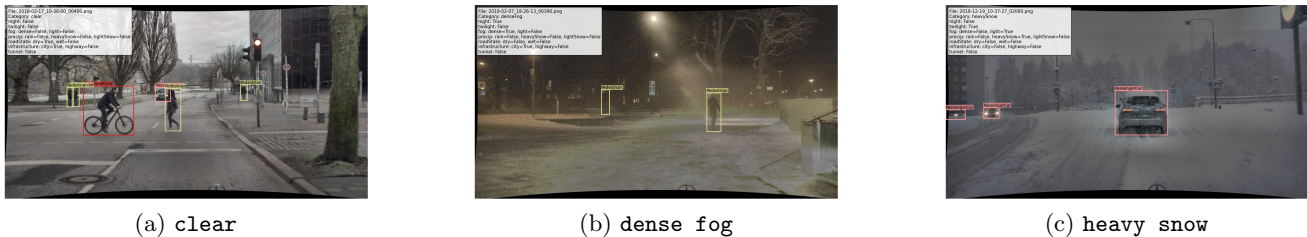


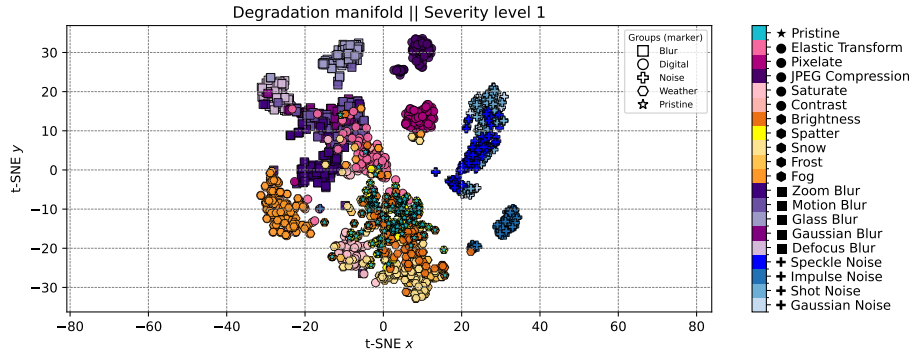
Figure 6: Examples from Seeing Through Fog (STF) [4] used for the natural weather-shift evaluation. We construct an ID split from clear/nominal scenes and OoD splits from adverse-weather conditions (*Dense Fog*, *Heavy Snow*, and *Heavy Rain* after filtering).



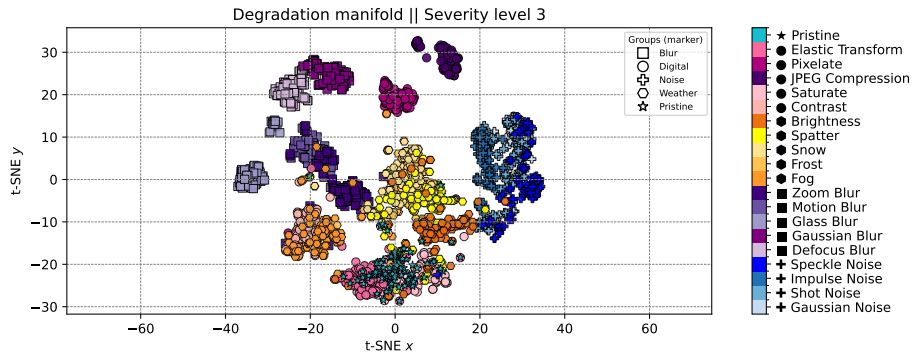
Figure 7: Examples from BDD100K [55] illustrating the weather-based ID/OoD construction. Left: ID example from the **clear** subset. Middle: ambiguous **rainy** example with weak cues (e.g., wet road only), which is excluded by manual refinement. Right: retained OoD example with strong visible rain cues (**heavy rain**).

Evaluation

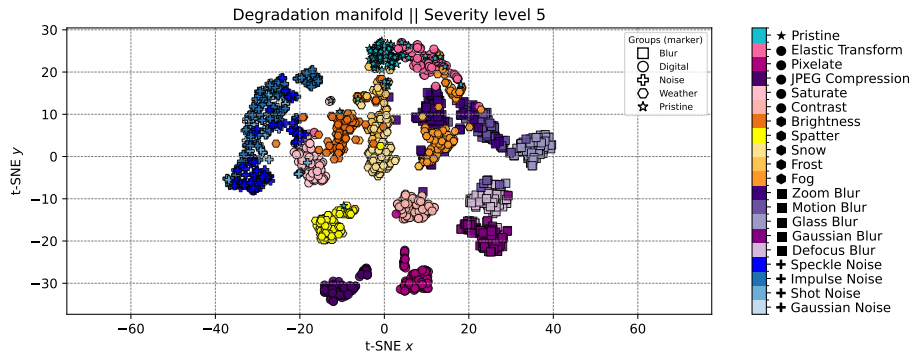
Figures 8 and 9 visualize the learned embedding space using t-SNE [19] for the degradation types from robustness evaluation ([36, 17]) and IQA-style degradations ([1]) for several severity levels. Across both corruption taxonomies, degraded samples form clearly separated clusters by degradation type despite the absence of degradation labels during training, indicating that the representation is primarily organized by degradation characteristics rather than semantic content.



(a) Severity level 1 (Hendrycks and Dietterich [17])

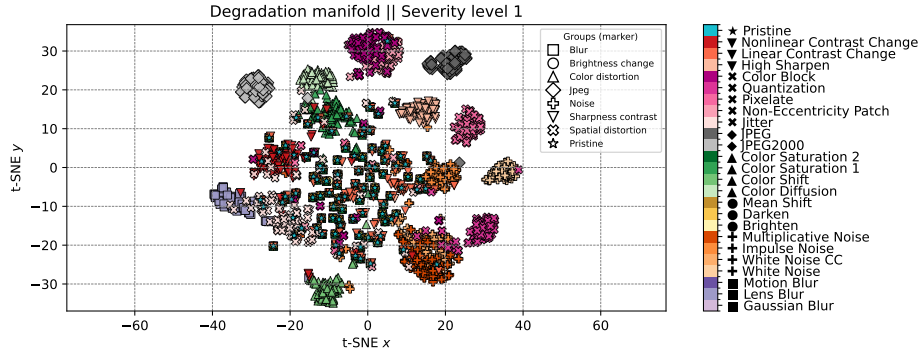


(b) Severity level 3 (Hendrycks and Dietterich [17])

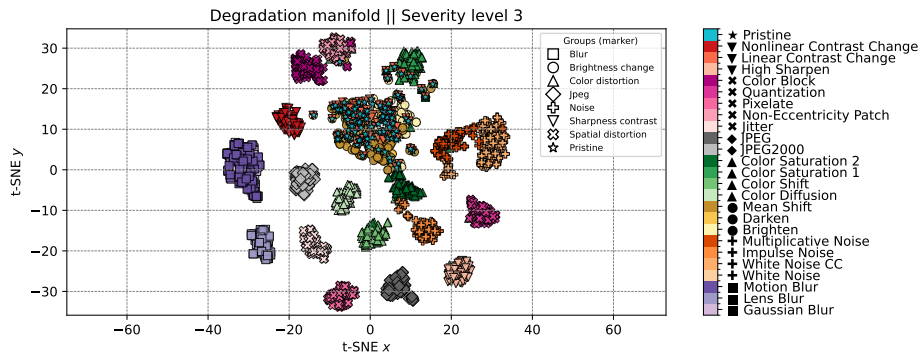


(c) Severity level 5 Hendrycks and Dietterich [17]

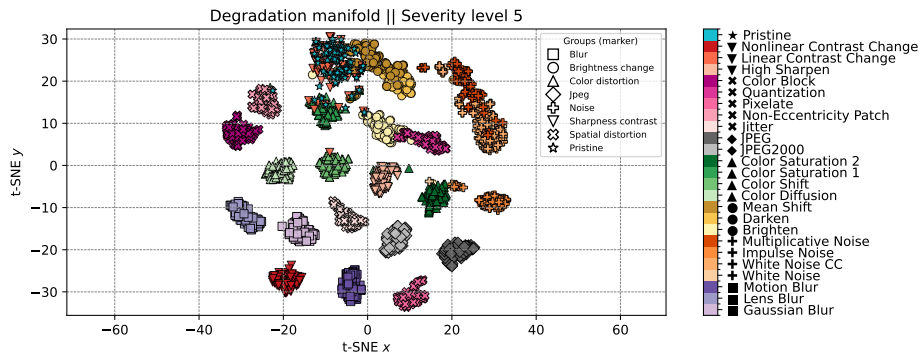
Figure 8: t-SNE visualization [19] of the learned degradation manifold under the corruption taxonomy of Michaelis et al. [36], based on [17], shown for three severity levels (1, 3, and 5). Each color denotes a specific degradation type, while marker styles indicate the corresponding degradation group. For visualization, 100 COCO [28] samples are corrupted at the respective severity level. At low severity (level 1), clusters begin to form but remain partially overlapping. With increasing severity (levels 3 and 5), degradation types become progressively more separated, indicating that the embedding geometry preserves a meaningful ordering with respect to degradation strength. Note that training used degradation compositions from Agnolucci et al. [1], demonstrating zero-shot generalization of the learned manifold.



(a) Severity level 1 (Agnolucci et al. [1])



(b) Severity level 3 (Agnolucci et al. [1])



(c) Severity level 5 (Agnolucci et al. [1])

Figure 9: t-SNE visualization [19] of the learned degradation manifold under the corruption taxonomy of Agnolucci et al. [1], shown for three severity levels (1, 3, and 5). Each color denotes a specific degradation type, while marker styles indicate the corresponding degradation group. For visualization, 100 COCO [28] samples are corrupted at the respective severity level. At low severity (level 1), clusters begin to form but remain partially overlapping. With increasing severity (levels 3 and 5), degradation types become progressively more separated, indicating that the embedding geometry preserves a meaningful ordering with respect to degradation strength.

Self-Awareness under Degradation

Probabilistic Detectors. The full results of the probabilistic detector [41, 15] are reported in 6 We evaluate nine probabilistic detector variants across three backbones and three scoring rules (ES, NLL, DMM). Across models, degradation shift is consistently reflected in detector outputs: predictive entropy and confidence distributions change systematically as severity increases. However, the quality and stability of these signals depend strongly on the training objective.

Energy Score (ES) variants yield more balanced predictive distributions under shift, whereas NLL-trained models often produce overly diffuse uncertainties and DMM variants tend to be overconfident. Interestingly, among all detector-derived signals, the raw confidence score consistently achieves the strongest AUROC, outperforming entropy- and covariance-based metrics. This behavior can be partially explained by the IoU-based objectives commonly used in detector training: predictive distributions are better calibrated for true positives than for false positives, and confidence values often remain the most separable quantity across severity levels. Moreover, aggregating only the top- k detections is preferable, as including all detections introduces poorly calibrated, low-quality hypotheses that obscure meaningful uncertainty signals.

Despite this sensitivity to shift, detector-derived monitoring exhibits fundamental limitations. All output-based signals depend on the presence and stability of object hypotheses and implicitly assume meaningful detections in the scene. Under strong degradations, detections may disappear or become unstable, limiting the reliability of image-level aggregation. Even the best-performing confidence-based variant remains clearly below our degradation-manifold approach.

In contrast, our method estimates degradation directly from backbone representations and is independent of object presence. Rather than modeling prediction uncertainty, it explicitly captures input-side covariate shift in representation geometry. This separation enables more stable degradations recognition across severity levels and detector architectures.

For the evaluation, we use the models and their probabilistic extensions by [15] ([code repository](#), last accessed February 2026). We either train on the COCO dataset [28] with the default hyperparameters and settings or use the provided COCO pre-trained weights. An input size of 640 is used throughout. For further details, we refer to the original publication.

Single-Degradation Analysis To further characterize the learned representation, we analyze separability for individual corruption types. Tables 8 and 7 report AUROC per degradation and severity level for (i) robustness-style corruptions from [17] and (ii) IQA-based degradations from [1]. The degradation manifold itself is trained exclusively on IQA-style degradations [1, 17].

Despite the fact that several evaluation degradations differ from those seen during contrastive training, the learned manifold preserves a consistent severity ordering: for most distortion types, separability increases monotonically with corruption strength.

This pattern suggests that the embedding encodes a structured degradation geometry that generalizes beyond the specific transformations encountered during training, enabling zero-shot generalization across both degradation types and parameterizations.

Score Distribution Figure 10 visualizes the effect of distributional shift for several corruption severity levels. In particular, the distribution of $S_{\text{deg}}(\mathbf{x})$ distance values for ID and OoD sets is shown using the proposed degradation manifold approach with a YOLOv10-m backbone.

Detector	Model	Severity levels AUROC \uparrow				
		1	2	3	4	5
FasterRCNN DMM	Trace	51.22	53.49	54.84	57.75	62.91
	Determinant	48.63	47.15	47.18	47.42	51.31
	Entropy (Regression)	50.71	52.55	53.85	57.77	62.40
	Confidence Score	53.51	59.04	60.50	67.91	71.23
	Entropy (Classification)	55.82	59.30	63.76	70.17	74.93
FasterRCNN ES	Trace	50.68	50.86	52.32	53.79	60.63
	Determinant	48.52	48.13	46.47	51.14	53.65
	Entropy (Regression)	52.87	53.36	56.70	57.41	61.34
	Confidence Score	55.18	58.82	63.10	64.94	73.20
	Entropy (Classification)	54.70	59.97	62.84	68.47	77.60
FasterRCNN NLL	Trace	52.84	51.43	53.40	54.91	58.77
	Determinant	47.62	46.72	49.00	43.65	51.91
	Entropy (Regression)	51.65	51.66	55.72	56.90	64.87
	Confidence Score	54.14	56.22	59.59	66.34	74.65
	Entropy (Classification)	53.31	59.65	64.35	70.43	77.33
DETR DMM	Trace	50.03	50.50	50.47	51.21	51.63
	Determinant	52.01	53.71	54.50	57.29	56.99
	Entropy (Regression)	49.78	50.87	48.74	49.67	50.62
	Confidence Score	53.79	56.10	59.04	66.47	71.17
	Entropy (Classification)	55.40	57.82	62.83	70.09	75.82
DETR ES	Trace	48.73	51.12	53.47	55.49	56.07
	Determinant	45.82	39.34	34.04	32.80	31.50
	Entropy (Regression)	49.94	55.67	58.25	61.90	63.13
	Confidence Score	51.31	56.26	58.92	64.96	70.05
	Entropy (Classification)	57.50	57.78	62.59	68.43	74.73
DETR NLL	Trace	51.14	54.83	58.96	59.68	63.61
	Determinant	45.81	45.06	47.58	51.58	51.93
	Entropy (Regression)	54.36	56.09	55.81	62.89	63.06
	Confidence Score	54.59	58.09	60.53	66.66	69.54
	Entropy (Classification)	55.11	59.33	63.08	69.14	74.09
RetinaNet DMM	Trace	53.04	53.18	55.46	59.73	64.39
	Determinant	49.32	51.49	47.22	51.91	49.41
	Entropy (Regression)	51.44	53.18	56.31	59.69	64.67
	Confidence Score	53.55	58.10	61.77	67.49	77.19
	Entropy (Classification)	51.34	49.72	51.92	53.83	51.49
RetinaNet ES	Trace	52.61	55.31	57.14	60.29	65.44
	Determinant	49.65	50.57	51.29	52.66	56.39
	Entropy (Regression)	52.73	55.15	57.67	60.82	66.51
	Confidence Score	52.55	56.77	60.72	68.10	75.28
	Entropy (Classification)	52.20	51.91	52.97	53.28	51.85
RetinaNet NLL	Trace	53.11	54.25	55.59	58.46	65.18
	Determinant	49.48	51.09	50.94	54.13	58.23
	Entropy (Regression)	53.37	54.12	57.55	62.49	66.10
	Confidence Score	52.91	56.93	61.51	69.69	77.65
	Entropy (Classification)	50.83	50.06	51.23	51.09	51.15

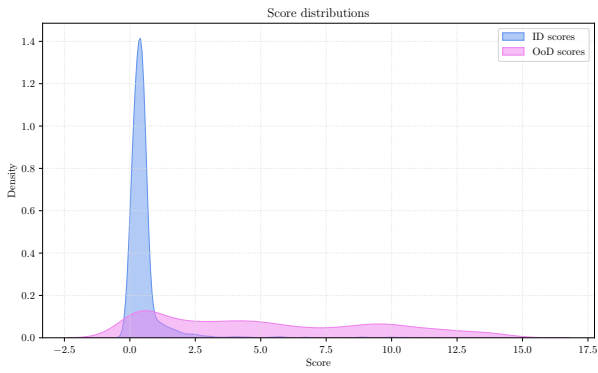
Table 6: AUROC scores for Top-3 detection uncertainties (as proposed from [41]) across using the probabilistic detector of [15] on synthetically corrupted versions of the COCO dataset.

Degradation Function [1]	Severity Levels AUROC \uparrow				
	1	2	3	4	5
'Gaussian Blur'	48.15	61.56	85.20	99.84	99.89
'Lens Blur'	98.02	98.45	98.90	99.20	99.50
'Motion Blur'	48.93	93.43	99.62	99.92	99.95
'White Noise'	98.38	99.28	99.60	99.75	99.85
'White Noise in Color Component'	85.23	98.72	99.36	99.70	99.85
'Impulse Noise'	80.02	98.93	99.70	99.80	99.88
'Multiplicative Noise'	92.25	98.02	99.16	99.40	99.60
'Brighten'	48.68	47.73	48.88	81.28	97.16
'Darken'	48.88	49.42	49.98	50.57	98.13
'Mean Shift'	48.16	50.37	50.70	62.20	64.77
'Color Diffusion'	96.51	98.08	98.04	98.56	98.15
'Color Shift'	95.60	98.75	98.85	99.04	99.20
'Color Saturation 1'	54.53	80.02	76.53	72.30	79.84
'Color Saturation 2'	48.81	75.74	93.54	98.17	98.50
'JPEG'	99.59	99.70	99.80	99.85	99.90
'JPEG2000'	98.83	99.75	99.85	99.92	100.00
'Jitter'	60.29	97.35	99.81	99.89	99.79
'Non-Eccentricity Patch'	85.95	94.67	96.89	97.66	98.05
'Pixelate'	97.17	99.92	99.95	99.96	100.00
'Quantization'	98.09	99.20	99.69	99.83	99.90
'Color Block'	86.04	94.54	97.12	98.04	99.22
'High Sharpen'	98.25	99.62	99.67	99.80	99.88
'Linear Contrast Change'	48.23	59.96	51.24	84.43	56.86
'Nonlinear Contrast Change'	60.39	97.10	99.17	99.71	99.78

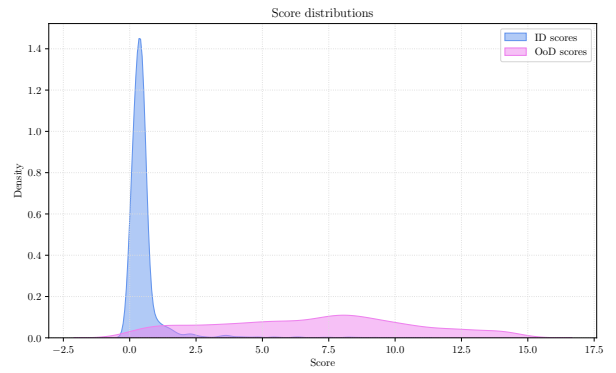
Table 7: AUROC for pristine–degraded separability under individual synthetic degradations on COCO. Degradations follow the IQA-style definitions of Agnolucci et al. [1].

Degradation Function [17]	Severity Levels AUROC \uparrow				
	1	2	3	4	5
'Gaussian Noise'	99.91	99.94	99.93	99.94	99.92
'Shot Noise'	99.63	99.74	99.83	99.81	99.85
'Impulse Noise'	99.96	99.94	99.92	99.91	99.90
'Speckle Noise'	99.70	99.72	99.73	99.72	99.71
'Defocus Blur'	99.86	99.87	99.88	99.87	99.86
'Gaussian Blur'	99.76	99.78	99.79	99.78	99.77
'Glass Blur'	99.98	99.97	99.96	99.95	99.94
'Motion Blur'	99.61	99.63	99.65	99.64	99.62
'Zoom Blur'	99.05	99.10	99.15	99.18	99.20
'Fog'	98.67	98.89	99.04	98.96	99.18
'Frost'	87.51	93.31	94.89	94.76	94.80
'Snow'	82.90	88.40	92.15	96.72	99.31
'Spatter'	54.95	60.55	86.97	99.77	99.92
'Brightness'	54.74	76.28	89.53	96.29	98.55
'Contrast'	98.78	99.16	99.32	99.41	99.47
'Saturate'	71.40	79.31	81.53	99.44	99.55
'JPEG'	99.99	99.98	99.97	99.96	99.95
'Pixelate'	99.96	99.95	99.94	99.93	99.92
'Elastic Transform'	92.72	92.83	90.84	84.89	88.96

Table 8: AUROC for pristine–degraded separability under individual synthetic degradations on COCO. Degradations follow the robustness benchmarks of Hendrycks and Dietterich [17] and Michaelis et al. [36].



(a) COCO-C1



(b) COCO-C5

Figure 10: Distribution of $S_{\text{deg}}(\mathbf{x})$ scores for ID and OoD samples at different corruption severity levels, using degradation manifold approach with a YOLOv10-m backbone.

Joint Detection–Degradation Training Study

In the main paper, we adopt an auxiliary two-path configuration in which the degradation manifold is trained independently from the detector’s primary objective. This preserves detection performance while enabling reliable degradation monitoring. In this section, we analyze the trade-off between detection robustness and degradation sensitivity under joint optimization.

Experimental Setup To keep computational cost manageable for this side study, we conduct experiments on COCO-mini [44], a stratified subset of COCO with preserved class distribution. Additionally, we evaluate a person-only subset (person instances larger than 40 pixels), where detection complexity is reduced and the effects of representation modification become more clearly observable.

We compare the following configurations using YOLOv10-m as backbone:

- **Default detector training:** Standard detection objective only.
- **Contrastive-only training:** Backbone fine-tuned solely with the degradation contrastive loss (no detection loss).
- **Naive multi-task training:** Joint optimization of detection loss and degradation contrastive loss using a simple weighted sum:

$$\mathcal{L}_{\text{total}} = \mathcal{L}_{\text{det}} + \lambda \mathcal{L}_{\text{deg}},$$

with fixed weighting λ .

Results

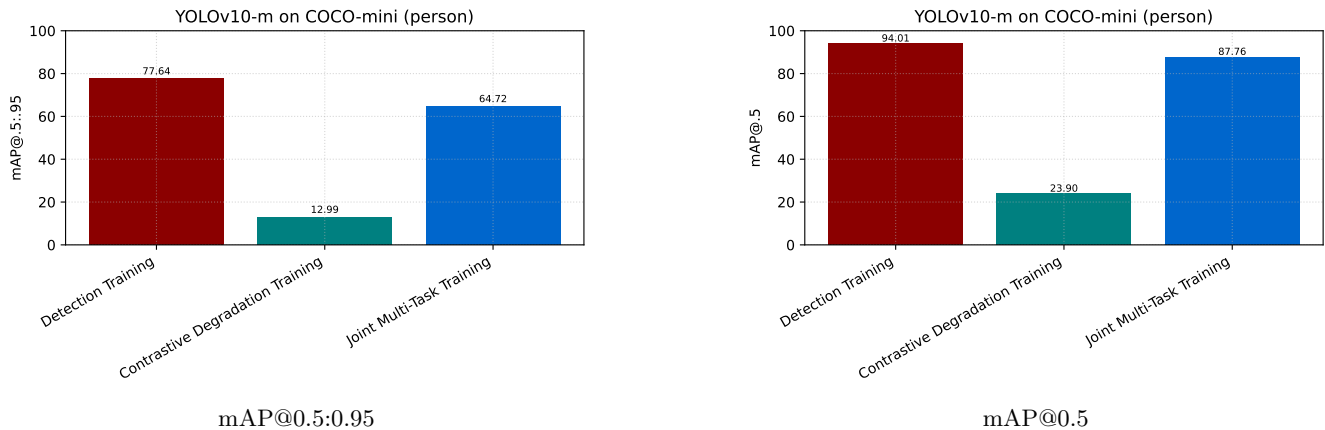


Figure 11: Detection performance of YOLOv10-m [48] under different training objectives on the COCO-mini person subset [44]. Detection-only training preserves baseline accuracy. Degradation-only training significantly disrupts semantic detection features. Joint multi-task optimization mitigates this effect while introducing a moderate performance trade-off.

Figure 11 shows the mAP (mAP@0.5:0.95 and mAP@0.5) comparison under different training objectives on the COCO-mini person subset [44].

The severe performance degradation under contrastive-only training is expected. The degradation objective explicitly promotes sensitivity to fidelity variations, whereas detection training encourages invariance to nuisance perturbations. Optimizing exclusively for degradation geometry therefore disrupts the semantic feature organization required for accurate object detection.

Naive multi-task training substantially mitigates this effect. Although a performance gap remains compared to the default detector, the model retains strong task performance while simultaneously learning structured degradation representations. This demonstrates that joint optimization is feasible, but introduces a measurable trade-off between detection invariance and degradation sensitivity.

Discussion These results highlight an inherent tension between invariance and sensitivity. Detection training aims to suppress sensitivity to nuisance degradations to preserve task performance. Degradation manifold learning intentionally amplifies sensitivity to fidelity variations to enable reliable monitoring.

The auxiliary two-path configuration used in the main experiments avoids this objective conflict and preserves full detection performance. The joint optimization results presented here indicate that more advanced balancing strategies (e.g., dynamic loss weighting, gradient projection, partial backbone freezing, or parameter-efficient adaptation) may further reduce the trade-off and represent promising directions for future work.

Training Details

This section provides implementation details of the degradation-manifold training procedure, including degradation composition, view generation, hard-negative construction, and the contrastive objective.

Degradation Sampling and Composition For each pristine training image $\mathbf{x} \sim \mathcal{D}$, we generate distorted views by sampling a *degradation composition*

$$\mathcal{C} = \{d_1, \dots, d_{n_{\text{deg}}}\},$$

i.e., an ordered sequence of degradation operators applied sequentially:

$$\mathbf{x}^{\text{deg}} = d_{n_{\text{deg}}}(\dots d_2(d_1(\mathbf{x}))).$$

The number of operators $n_{\text{deg}} \in \{1, \dots, N_{\text{deg}}\}$ is sampled uniformly. Each operator is drawn from a predefined pool of degradation groups (blur, noise, compression, brightness, color distortion, spatial distortion, sharpness/contrast), following the grouping strategy of Agnolucci et al. [1] or weather effects as described in Hendrycks and Dietterich [17]. At most one operator per group is selected within a composition following [56, 59, 1]. The order of selected operators is randomly shuffled, and each operator is parameterized by a randomly sampled severity level.

This stochastic chaining yields a large variety of structured degradation regimes while preserving semantic content. Importantly, evaluation corruptions follow robustness-style taxonomies and partially differ from the training degradations, resulting partly in a zero-shot generalization setting. The degradation composition is visualized in Figure 12

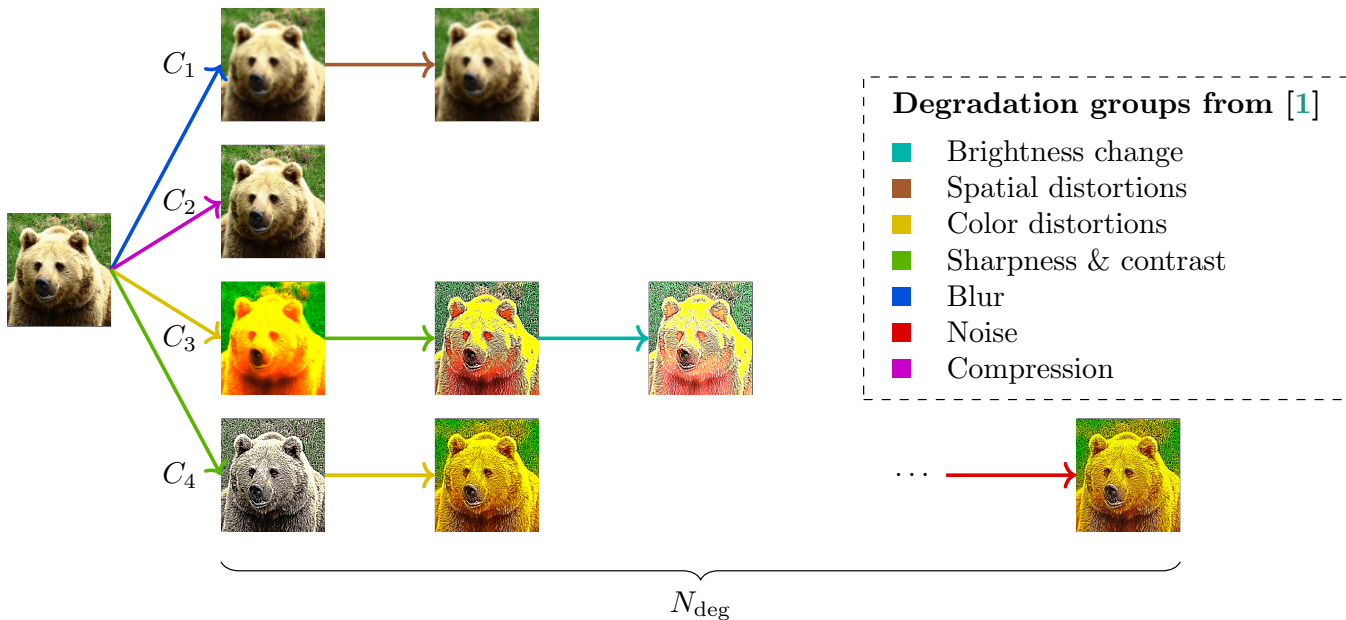


Figure 12: Overview of the applied image degradation model. Randomly assembled degradation compositions \mathcal{C} are applied sequentially to synthesize diverse degradation patterns. Each degradation composition contains up to N_{deg} degradations sampled from pre-defined degradation groups (e.g., the degradation groups of Agnolucci et al. [1]).

View Generation For each sampled composition \mathcal{C}_i , we generate two independently parameterized degraded views:

$$(\mathbf{x}_{i,A}^{\text{deg}}, \mathbf{x}_{i,B}^{\text{deg}}).$$

Both views share the same operator sequence but differ in sampled parameters (e.g., blur kernel size, noise variance). This enforces invariance within a degradation regime while preserving regime identity.

All images are resized to the detector’s default input resolution (e.g., 640×640) before feature extraction.

To strengthen discrimination between subtle fidelity changes, we construct additional *hard negatives*. For each degraded view, we extract a centered crop covering half the spatial extent (i.e., reduced width and height), and subsequently resize it back to the detector’s default input resolution:

$$\tilde{\mathbf{x}}^{\text{deg}} = \text{Resize}\left(\text{CenterCrop}_{1/2}(\mathbf{x}^{\text{deg}})\right).$$

This procedure introduces resolution-induced information loss due to downsampling before resizing, while largely preserving semantic content. An overview of this training strategy is shown in Figure 13.

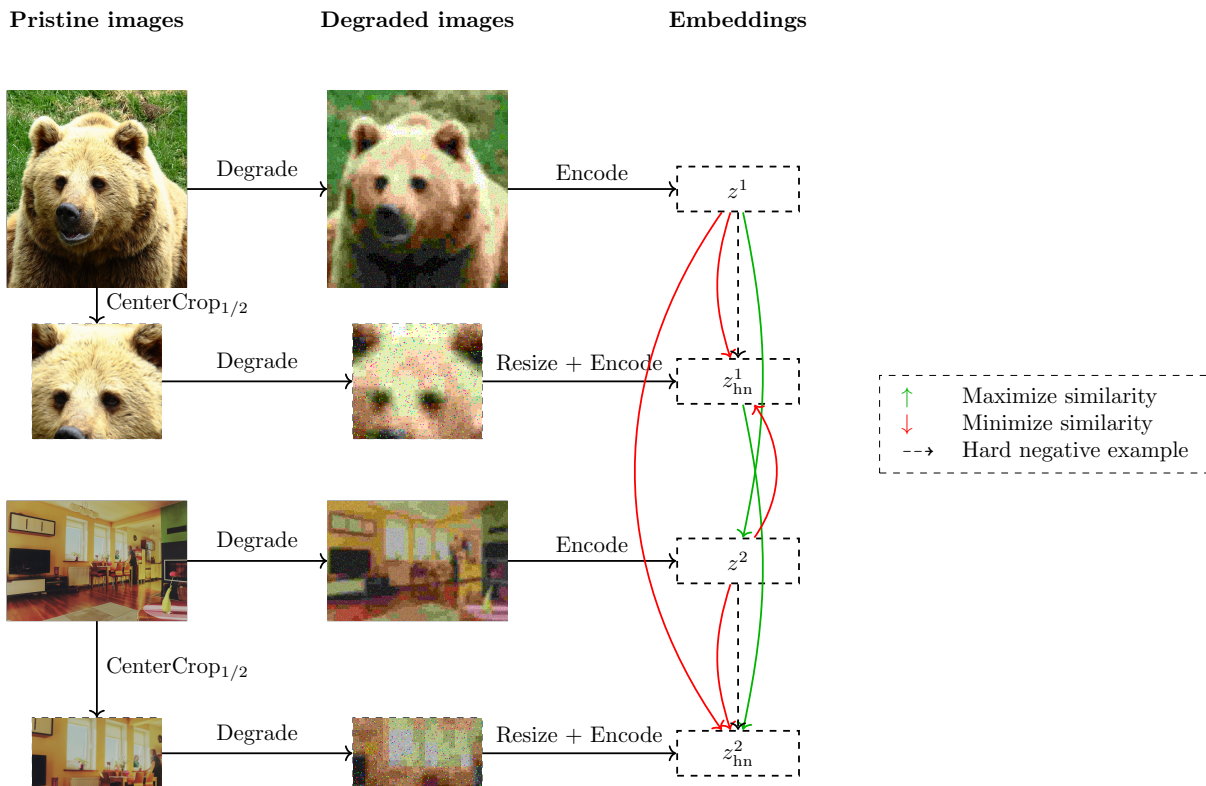


Figure 13: Training pair construction for degradation-manifold learning. Two pristine images are degraded using the same sampled composition, forming a positive pair in embedding space (z^1, z^2). To construct hard negatives, we apply an additional half-size crop before resizing to the detector input resolution. All degraded views are resized to the detector’s default input size prior to encoding. The objective pulls embeddings of equally degraded full-resolution images together while pushing them away from their resolution-perturbed counterparts, encouraging sensitivity to fidelity changes beyond semantic similarity.

Contrastive Objective Let z_i^A and z_i^B denote embeddings of the two degraded full-resolution views for sample i , and \hat{z}_i^A, \hat{z}_i^B the corresponding hard-negative embeddings. Embeddings are obtained from the detector backbone followed by a projection head.

For a batch of size B , we employ the NT-Xent loss [5] with cosine similarity and temperature τ . Define

$$\gamma(a, b) = \exp\left(\frac{\cos(a, b)}{\tau}\right).$$

Each full-resolution pair (z_i^A, z_i^B) forms a positive pair, while all other embeddings in the batch—including hard negatives—serve as negatives.

The per-sample loss term is

$$\ell_i^{A,B} = -\log \frac{\gamma(z_i^A, z_i^B)}{\sum_{k=1}^B [\gamma(z_i^A, z_k^B) + \gamma(z_i^A, \hat{z}_k^B) + \gamma(z_i^A, \hat{z}_k^A)] + \sum_{k \neq i}^B \gamma(z_i^A, z_k^A)}.$$

Symmetric terms are defined analogously for (B, A) and for the hard-negative anchors. The final loss is

$$\mathcal{L} = \frac{1}{4B} \sum_{i=1}^B [\ell_i^{A,B} + \ell_i^{B,A} + \hat{\ell}_i^{A,B} + \hat{\ell}_i^{B,A}].$$

This objective pulls embeddings of identically composed degradations together while pushing apart different compositions and resolution-perturbed hard negatives, thereby structuring the embedding space according to degradation regimes.